LASER FLASH SPECTROSCOPY OF ZINC/RUTHENIUM MYOGLOBINS: AN INVESTIGATION OF DISTANCE AND MEDIUM EFFECTS OF PHOTOINDUCED LONG-RANGE INTRAPROTEIN ELECTRON TRANSFERS

Thesis by

Andrew William Axup

In Partial Fulfillment of the Requirements

for the Degree of

Doctor of Philosophy

California Institute of Technology

Pasadena, California

1987

(Submitted 19 November 1986)

ACKNOWLEDGMENT:

I would like to extend my sincerest appreciation to those who assisted me through my graduate years. With especial pleasure, I would like to thank my advisor, Harry Gray, for allowing me the opportunity to participate in his research group. Open interaction and boundless enthusiasm are among the hallmarks of the ever-memorable Gray Group. I wish also to thank the Fannie and John Hertz Foundation for its generous financial support throughout my graduate career.

Of the many daily contributions from the members of the bio and photo groups, I would like to particularly thank Mike Albin, Jenny Karas, and Charlie Lieber for their time and comments during the composition of proposals and this thesis. I greatly value and admire the technical expertise of Tom Dunn, by whose efforts, even the most serious equipment failure was soon rectified.

Finally, I would like to thank my friends, family, and above all, my parents for their unending faith that this thesis would indeed ever be written.

To Nannie

ABSTRACT:

An experimental investigation of the distance dependence of long-range intramolecular electron transfer in ruthenium-modified zinc myoglobins has been performed. The zinc/ruthenium-modified metalloproteins were prepared by substitution of zinc-mesoporphyrin IX diacid (ZnP) into four previously characterized pentaammineruthenium(III) (a_5Ru) derivatives of sperm whale myoglobin (Mb). The derivatives are a_5Ru(His-48)Mb, a_5Ru(His-12)Mb, a_5Ru(His-116)Mb, and a_5Ru(His-81)Mb. Pulsed laser excitation of the zinc myoglobin produces the long-lived and highly reducing triplet excited state ($^3ZnP^*$). Electron transfer from this triplet to the ruthenium, $^3ZnP^*$-$Ru^{3+} \rightarrow ZnP^+$-$Ru^{2+}$ ($\Delta E^\circ \cong 0.8$ V), was measured by time-resolved transient absorption techniques. The observed electron-transfer rates are 7.0×10^4, 100, 89, and 85 s^{-1} for the His-48, -12, -116, and -81 derivatives, respectively, at 25°C. The electron-transfer distances were evaluated using computer modelling in which rotation about the C_α-C_β bond of the imidazole side chain in the ruthenium-modified histidines is restricted by nonbonded repulsions with atoms at the protein surface. Recent crystallographic results for a_5Ru(His-48)Mb indicate that the histidine has considerable rotational flexibility. The estimated accessible distances, both heme edge to inner coordination sphere ligand (e-e) and metal-to-metal (m-m), are as follows. For the His-48 derivative, the e-e range is 13.4-16.6 Å and the m-m range is 18.6-24.1 Å; His-12 ranges are 22.1-22.4 Å and 28.8-30.4 Å; His-116 ranges are 18.9-20.4 Å and 23.1-27.8 Å; and His-81

ranges are 19.0-19.4 **A** and 26.3-26.9 **A**. In addition, the orientation angles (Θ) of the electron-transfer pathways with relation to the heme plane at a position of closest approach are 25° (His-48), 20° (His-12), 35° (His-116), and 25° (His-81). Fitting the rate data to an exponential distance dependence yields the expression $k_{et} = 8x10^9 \exp(-\beta(R-4))\ s^{-1}$, where $\beta = 1.2\ A^{-1}$ and $R - 4 \geq 0$ (R is the minimum e-e distance in **A**). The electron-transfer rate in a_5Ru(His-12)Mb(ZnP) is anomalously high (100 vs. 2 s^{-1} predicted by the rate-distance equation), thereby indicating that the $^3ZnP^*$-Ru^{3+} electronic coupling may be enhanced by an intervening tryptophan residue that lies parallel-planar to the heme along the reaction pathway. Activation enthalpies calculated from the temperature dependences of the electron-transfer rates over the range 5-40°C are 1.7 ± 1.6 (His-48), 4.7 ± 0.9 (His-12), 5.4 ± 0.4 (His-116), and 5.6 ± 2.5 (His-81) kcal mol^{-1}. Dynamic flexibility of the protein region containing His-48 may reduce the activation enthalpy with respect to the other more rigidly located derivatives.

TABLE OF CONTENTS:

LIST OF FIGURES:

LIST OF TABLES:

CHAPTER I

Introduction

Electron transfers are important mechanistic steps in biologically significant processes such as photosynthesis and respiration.[1-4] Many of the these reactions are catalyzed by metalloenzymes that contain several protein-bound metal centers. The metal centers may function as electron-transfer sites and/or substrate-binding loci.

In these multisite proteins, the metal centers often are separated by long distances (>10 Å).[5] At such distances, electronic interactions are expected to be weak and electron-transfer rates should be correspondingly slow. At these long distances, however, rapid electron-transfer rates have been observed, notably in the photosynthetic reaction centers.[6]

These somewhat unexpected results, as well as the fundamental importance of electron-transfer reactions in biological processes, have stimulated both theoretical and experimental investigations to elucidate the factors that govern electron-transfer kinetics. These factors include the distance between the electron-transfer sites, the thermodynamic driving force of the overall reaction, the inner sphere reorganization, the spatial orientation of the donor and acceptor, and the nature of the intervening medium.

Several experimental approaches have been taken in an attempt to elucidate the contributions of these parameters to the rates of electron transfer. Early work involved the study of bimolecular quenching between various donors and acceptors.[7] The electron-transfer kinetics were observed by donor fluorescence quenching by acceptors in fluid solution. Increasing the driving force produced increased quenching rates until a plateau was reached. The plateau was attributed to dif-

fusion limiting factors in the bimolecular processes. Attempts to control the effects of diffusion involved studying the electron-transfer reactions in a rigid matrix.[8,9] The donors and acceptors were randomly distributed at fixed distances, requiring rather elaborate calculations to determine the electron transfer rates.

Intermolecular reactions of inorganic complexes with metalloproteins have been studied. From the rates observed in these experiments, the electron-transfer distance was determined by utilizing a bimolecular mechanistic model that featured close approach of the inorganic complex to the protein redox site.[10,11] Though the results agreed reasonably well with estimates of the metalloprotein redox site-to-surface distance evaluated from molecular models, the actual contact point was not known. Without this information, a reliable description of the distance, orientation, and intervening medium associated with the reaction pathway is lacking.

In order to circumvent the disadvantages of the intermolecular systems and to allow greater control in governing the selective variation of factors that influence electron transfer, well-defined unimolecular systems have been sought. Initial studies involving a linked porphyrin-quinone system established the utility of this class of structure in investigations of intramolecular fluorescence quenching.[12] Similar work has involved a polypeptide chain as a bridge between two redox centers.[13,14] In both cases, the linking frame was nonrigid, and a definitive determination of separation distance and orientation was not obtained.

Numerous fixed-site systems have recently been synthesized.

Rigid linkers have been incorporated in several donor-acceptor systems.[15-19] A through-bond electron-transfer mechanism was proposed in many of these systems and recent theoretical work has indicated that a network of carbon-carbon σ-bonds facilitates electron transfer through an aliphatic bridge.[20] These investigations have provided insight into the mechanisms operating in systems where the through-bond and through-space pathway lengths are nearly the same. In many biological processes, however, long-range intraprotein electron transfer appears to occur through a noncovalently linked medium. An understanding of the protein medium and the mechanisms that operate during intraprotein electron transfer requires the utilization of metalloproteins in further studies.

Several successful strategies have been employed to obtain two-site metalloprotein systems with fixed distances and orientations. Knowledge of the crystallographic structure of the protein allows the characterization of the intersite distance, orientation, and intervening medium. One approach has involved the association of two physiologically matched proteins to form a multisite protein-protein complex.[21-24] This method may require computer-graphics simulation to generate the docked complex's three-dimensional structure if the protein-protein structure is not known. An alternative approach to the study of long-range intraprotein electron transfer has centered on two-site systems in which a redox active species is attached to a specific location on a single-site metalloprotein. The latter strategy is the focus of this work.

The selection of the inorganic redox agent is based on two

criteria. First, the complex must react with some specificity at the protein surface. And second, the complex must be substitutionally inert in the relevant oxidation states. The reaction of pentaammineaquoruthenium(II) ($a_5Ru(H_2O)$) with the imidazole side chain of a histidine residue has been employed in earlier studies on protein conformation.[25,26] This methodology has been successfully employed in studies of long-range intraprotein electron transfer in ruthenium-modified derivatives of horse heart cytochrome *c* and *Pseudomonas aeruginosa* azurin.[27-30] The site of ruthenium attachment was determined by tryptic digestion of the protein and subsequent analysis of the resulting peptide fragments. In agreement with computer-modelled surface accessibility predictions, only one histidine site was labelled in each of these two proteins. Crystallographic structures of the native proteins allowed the evaluation of the intersite distances and orientations. In addition, the intervening medium was examined. These well-defined and characterized systems have provided important kinetic data, but as the proteins contain only one accessible modification site, they are unsuitable for studying distance and orientation effects.

By selecting a metalloprotein with multiple surface-accessible histidines, more than one rate-distance relation could be determined. For this reason, sperm whale myoglobin was chosen for ruthenium modification. As indicated in Figure 1, four histidines are available for ruthenium labelling. The four singly-modified derivatives have been prepared and characterized.[31,32] In previous studies, the intramolecular electron-transfer rate between the ruthenium label at the

Figure 1. Structure of sperm whale myoglobin (α-carbon chain). Surface-accessible histidines are indicated. Distances from the porphyrin edge to the imidazole ring are 13 Å (His-48), 19 Å (His-81), 20 Å (His-116), and 22 Å (His-12).

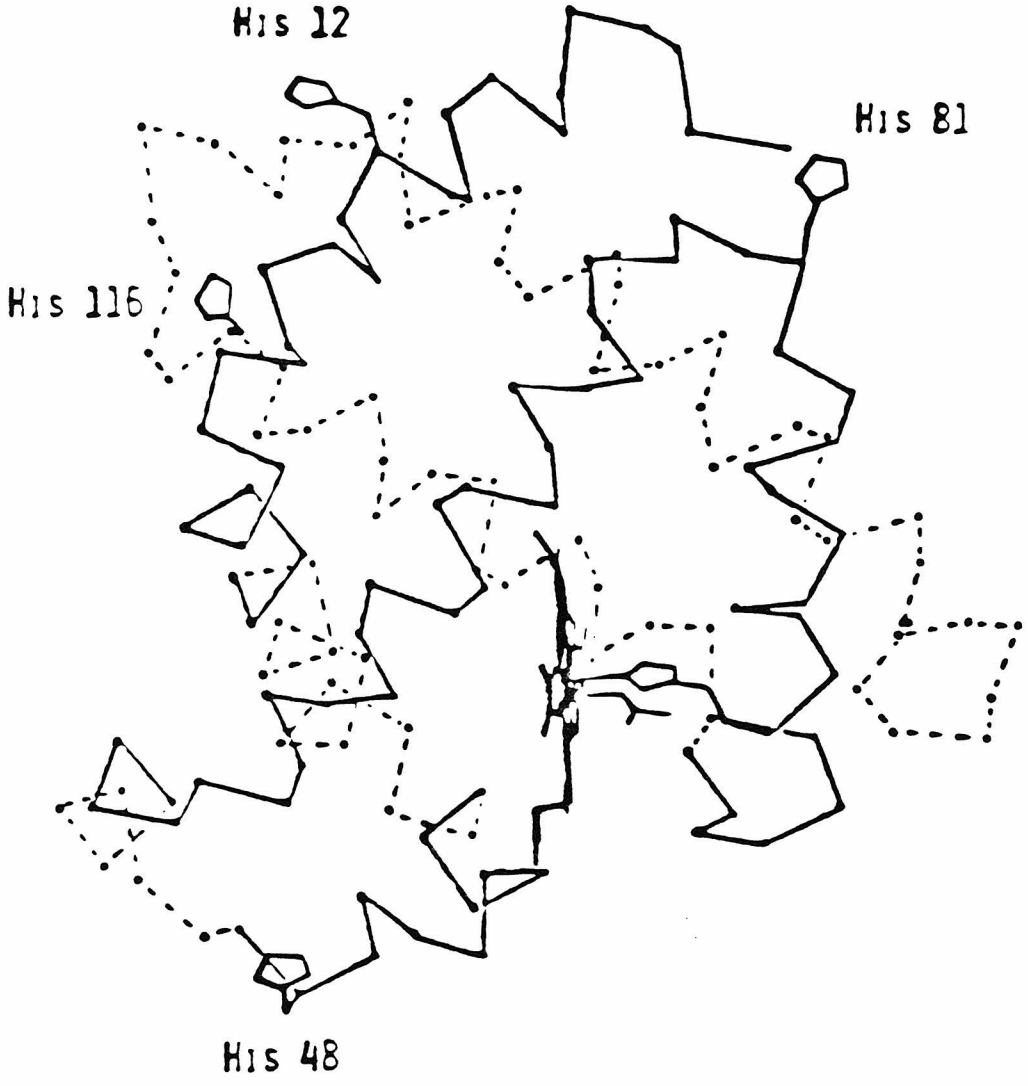
His 12
His 81
His 116
His 48

histidine-48 residue and the heme iron has been determined.[32,33] Experimental determination of the intramolecular electron-transfer rates at the three longer distances has not been possible because the overall reaction, $Fe^{2+} \rightarrow Ru^{3+}$, is very slow at low driving force (ΔE° = 0.02 V).

In this work, the "ruthenated" myoglobin system was modified in order to increase the driving force so that the electron-transfer rates to all four ruthenium-labelled histidines could be determined. The excited triplet zinc porphyrin ($^3ZnP^*$) is a good reducing agent and has been utilized as an electron donor in long-range electron-transfer studies.[21-24] Substitution of the zinc porphyrin for the heme in the ruthenium-modified myoglobins produces the desired multisite (multidistance) systems. Photoexcitation generates a long-lived triplet that can reduce the histidine-bound ruthenium(III) (ΔE° ~ 0.8 V). The porphyrin cation radical (ZnP^+) then can oxidize the ruthenium, returning the system to its initial state (Scheme 1).

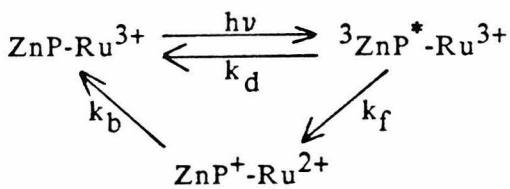

Scheme 1.

Utilizing these zinc/ruthenium-modified myoglobins, the electron-transfer rates over the distance range 13 - 22 Å were measured by transient absorption methods. Changes in other factors, such as

driving force and inner sphere reorganization, are minimized by utilizing the same donor ($^3ZnP^*$) and acceptor (a_5Ru) in the four different derivatives.

Having obtained kinetic data for the zinc/ruthenium-modified myoglobins, an accurate assessment of the site separation was needed to complete the rate-distance relation. A computer-graphics image of the surface regions of each modified histidine was examined to evaluate the degree of rotational flexibility accessible to the histidine residues. Nonbonded repulsions of the ruthenium-modified imidazole side chain with the protein surface limit the rotational range of the residue. From these interactions, a minimum approach distance can be estimated. The intervening medium of each electron-transfer pathway was examined as well as the orientation of each pathway with respect to the porphyrin plane. Based on this information, a detailed description of the various electron-transfer parameters and an evaluation of the change in each parameter can be presented. The kinetic data can now be correlated within a well-defined system of distance variations.

CHAPTER II

Experimental

Materials and Apparatus:

Distilled water, filtered through a Barnstead Nanopure water purification system (No. 2794, specific resistance > 18 MΩ-cm), was used in the preparation of all aqueous solutions. Hydrochloric acid (Mallinckrodt), nitric acid (Baker), perchloric acid (Baker, 60%), and sulfuric acid (Mallinckrodt) were used as received. Aqueous base solutions were prepared from reagent grade sodium and potassium hydroxide (Baker) and sodium bicarbonate (Baker). Sodium chloride (Baker) and sodium dithionite (MCB) were used as obtained. 2-Butanone (MCB) was stored over aluminum oxide (Woelm neutral, Waters Associates) at 4°C to prevent the accumulation of peroxides. Other organic solvents, chloroform (Baker), N,N-dimethylformamide (MCB), ethanol (U.S. Industrials, absolute), ethyl acetate (Burdick and Jackson), methanol (Baker, absolute), pyridine (Mallinckrodt), and toluene (Burdick and Jackson), were used as received.

Tris(hydroxymethyl)aminomethane buffer solutions were prepared from reagent grade Trizma hydrochloride and base (Sigma). A μ = 0.05 M, pH 7.2 (25°C), 7.8 (5°C) buffer solution was prepared according to the manufacturers specification (28.08 g of Trizma HCl, 2.68 g of Trizma base, 4 L of water). A μ = 0.1 M buffer solution was obtained by doubling the quantities of Trizma salts used as described above.

Phosphate buffer solutions were prepared from reagent grade mono- and dibasic sodium phosphate salts (Mallinckrodt). A μ = 0.1 M, pH 7.0 (25°C) buffer solution was prepared by general reference specifications (10.85 g of sodium phosphate monobasic ($NaH_2PO_4 \cdot H_2O$), 15.20 g of sodium phosphate dibasic (Na_2HPO_4 (anhydrous), 4 L of water).[34] A

μ = 0.01 M, pH 7.0 (25°C) buffer solution was prepared by diluting (1:9, buffer/water) a μ = 0.1 M, pH 6.7 solution (18.08 g of $NaH_2PO_4 \cdot H_2O$, 12.73 g of Na_2HPO_4 anhyd., 4 L of water).

Carboxymethyl cellulose cation exchange resin, CM-52 (Whatman, pre-swollen, microgranular), was equilibrated as indicated by the manufacturer (six aliquot buffer changes). Following equilibration, the settled resin volume was increased by 20% with buffer to form a slurry, poured into a column, and allowed to settle for several hours. Five column volumes of buffer were passed to pack the column prior to use. CM-52 resins were cleaned after use by washing with a high-salt solution (~1-3 M NaCl). Sephadex ion exchange gel, G-25-80 (Sigma, bead size 20-80 μ) was equilibrated in the desired buffer, slurried and poured in a fashion similar to that described for CM-52. Sephadex gels were cleaned by multiple washings with buffer or water.

Samples were degassed and purged with purified argon (passed through a manganese oxide column) on a dual manifold vacuum-argon line. At least five vacuum/purge cycles were used to deoxygenate samples. Transfers were done anaerobically with a cannula (Aldrich, 20 ga. stainless, non-coring tips). Other air sensitive manipulations were performed under argon in a Vacuum Atmospheres Co. HE-43-2 Dri Lab inert atmosphere box. Concentration of protein solutions and removal of small molecules were achieved with an Amicon ultrafiltration system (YM-5 filter, 5000 molecular weight cutoff). A Gilson Minipuls 2 peristaltic pump with 0.32 mL/m tubing was used to regulate buffer flow through some chromatographic columns. A setting of 400 provides a flow rate of about 30 mL/h.

Sample and spectrophotometric cells were cleaned by multiple washings with water. Periodically, cells were washed with 3:1 (v/v) hydrochloric acid/nitric acid, followed by concentrated sulfuric acid, and then rinsed with water until constant pH was reached. Cells were either air or vacuum dried.

Preparations and Purifications:

General Materials:

The perchlorate[35] and chloride[36] salts of tris-(1,10-phenanthroline)cobalt(III), $Co(phen)_3^{3+}$, were prepared by literature methods. A saturated solution of $Co(phen)_3^{3+}$ was used to oxidize the protein samples.

Pentaammineaquoruthenium(II) was synthesized by reduction of chloropentaammineruthenium(III) (Strem) by zinc amalgam.[37] Zinc amalgam was prepared from zinc metal (Mallinckrodt) and a saturated aqueous mercuric chloride (Mallinckrodt) solution. The product was precipitated as the hexafluorophosphate salt and stored under vacuum dessication or used directly in the labelling reaction with protein.

Purification of sperm whale skeletal muscle ferrimyoglobin:

In 20 mL of Tris buffer (μ = 0.05 M, pH 7.2), 6 g of Sigma ferrimyoglobin, metMb, were dissolved. The protein solution was centrifuged to separate the insoluble material. The supernatant was applied to a CM-52 column (4 cm x 80 cm) equilibrated with Tris

buffer (μ = 0.05 M, pH 7.2) at 4°C. The sample was eluted at 50 mL/h with Tris buffer (μ = 0.05 M, pH 7.2). Four separable bands were typically observed, and Band IV (the richest in metMb) was used for these studies.

Preparation of pentaammineruthenium(III)ferrimyoglobin:[33]

A solution containing 600 mg (25 mL of 1.3 mM metMb) of ferrimyoglobin in Tris buffer (μ = 0.05 M, pH 7.2) was degassed and purged with argon in a septum-stoppered 120 mL bottle. Excessive foaming of the protein solution when degassing was avoided because it denatures the protein. 130 mg of degassed pentaammineaquoruthenium(II) hexafluorophosphate were dissolved in 15 mL of argon-purged Tris buffer (μ = 0.05 M, pH 7.2).

The pentaammineaquoruthenium(II) was transferred under argon to the ferrimyoglobin solution. The ferrimyoglobin was immediately reduced to the ferro- species and the solution changed color from brown to deep red. After the mixture had reacted without agitation at room temperature for thirty minutes, the reaction was quenched by elution on a Sephadex G-25-80 column (phosphate buffer, μ = 0.1 M, pH 7.0). The protein fraction was collected, oxidized with $Co(phen)_3^{3+}$, and stored at 4°C.

Purification of pentaammineruthenium(III)ferrimyoglobin:[32,33]

The mixture of ruthenated myoglobins was desalted by five cycles of Amicon concentration and dilution with water, and then reduced to a final volume of 6 mL (600 mg, 5.6 mM modified metMb). The modified

myoglobins were separated by isoelectric focusing. An LKB system (2117 Multiphor, 2197 Electrofocusing Power Supply) was used. Two gels were prepared by standard procedures,[38] except that the ampholine solutions were passed through an Amicon YM-5 filter to remove any high molecular weight ampholytes. This procedure facilitated the removal of the remaining low molecular weight ampholytes from the protein solution following focusing.

To each gel, 3 mL of protein solution were applied, and the gels were run at 4°C (power supply settings: 1500 V, 22 mA, 10 W). Progress of the focusing was monitored visually by observing the separation of the modified myoglobin bands. When sufficient resolution of native, singly-modified and doubly-modified bands occurred, the gels were stopped. The band of singly-modified derivatives was scooped from the trays and eluted from the gel with water through a disposable frit. The ampholytes were removed from the collected protein solution by Amicon ultrafiltration.

The mixture of singly ruthenated myoglobin derivatives was concentrated and loaded onto a CM-52 column (equilibrated with μ = 0.1 M Tris buffer, pH 7.2, 4 cm x 70 cm) at 4°C. The protein was eluted with Tris buffer at 50 mL/h. Four bands were collected and each was concentrated and rechromatographed, if necessary. Fractions were kept at 4°C for short-term storage or frozen at -60°C (0.1 mM protein) in Tris buffer. $Co(phen)_3^{3+}$ was added to all modified protein solutions for storage. The order of elution from the CM-52 column was His-12, His-116, His-81, and His-48.[31,32]

Preparation of zinc-mesoporphyrin IX diacid:

The porphyrin dimethyl ester was first saponified to the diacid (Figure 2). 250 mg of mesoporphyrin IX dimethyl ester (Sigma) were dissolved in 5 mL of pyridine in a 50 mL three-neck flask. The flask was wrapped in foil and placed under an argon flow. 20 mL of 1% potassium hydroxide in methanol (0.29 g KOH (89%) in 25 mL MeOH) were added with 3 mL of water. The reaction mixture was heated and refluxed for two hours. 6 N hydrochloric acid was added to precipitate the porphyrin diacid. The reaction mixture was refrigerated overnight. The sample was centrifuged and decanted.

Zinc(II) was inserted into the free base by literature methods.[39] The diacid was dissolved in 15 mL of N,N-dimethylformamide and heated to reflux. 0.5 g zinc chloride (Mallinckrodt) was added. After 15 minutes, an absorption spectrum was taken (Figure 3). If any free base remained, an aliquot from a saturated solution of zinc chloride in dimethylformamide was added.

The precipitated solid was washed with water several times to remove all traces of pyridine. The zinc-mesoporphyrin IX diacid was dried under vacuum. If the porphyrin did not dry completely, residual pyridine was the likely cause. The pyridine was removed by redissolving the porphyrin in hot N,N-dimethylformamide and filtering the insoluble material on a medium frit. The solution was cooled, ice water was added, and the sample was stored overnight at -20°C.

Evaluation of the completeness of the reaction and purity of the product was done by thin layer chromatography (EM Reagents, silica gel 60 F_{254}). Samples were spotted from chloroform solution and an

Figure 2. Structure of porphyrin IX. Differing groups are indicated for proto and meso forms.

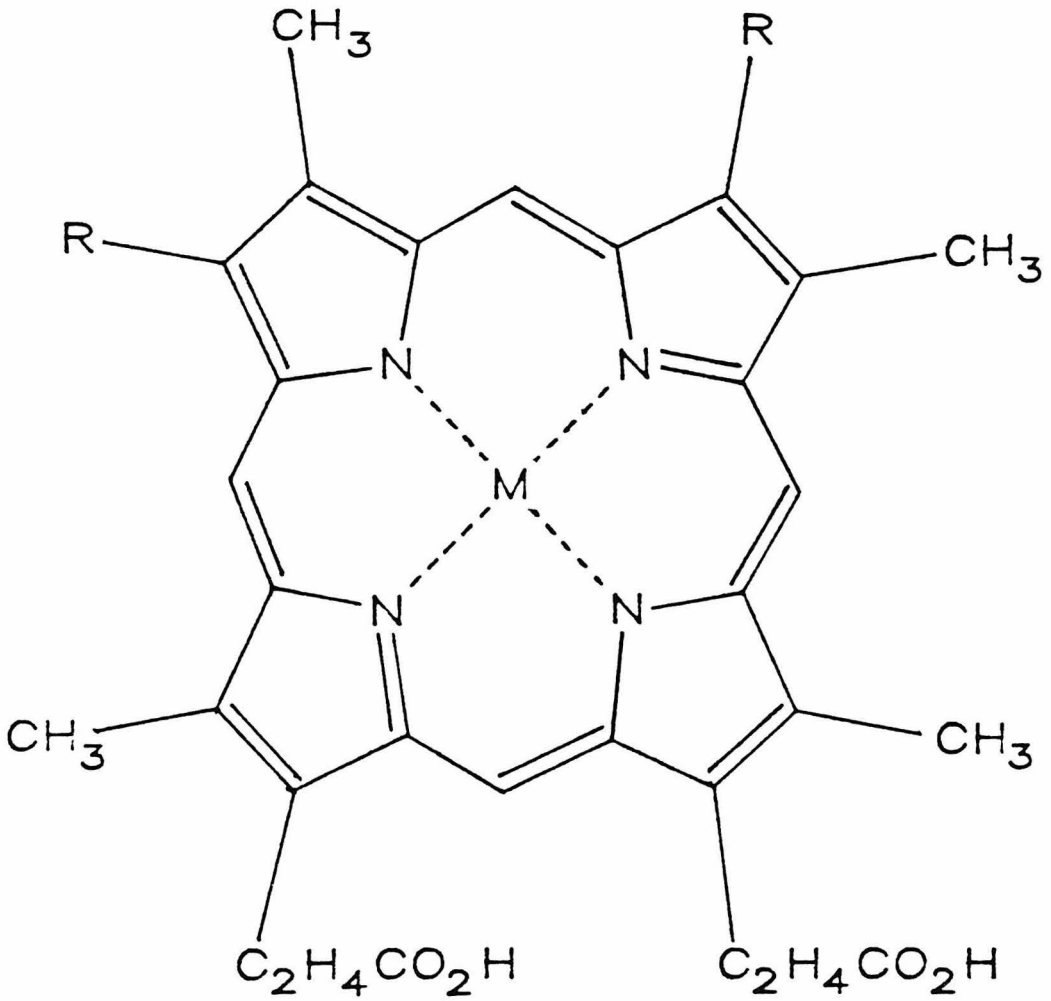

Proto: R = C_2H_3

Meso: R = C_2H_5

M (metal): Fe, Zn

Figure 3. Absorption spectra of mesoporphyrin IX (top) and zinc-mesoporphyrin IX (center) in DMF. Spectrum of Mb(ZnP)(aq) is included for comparison.

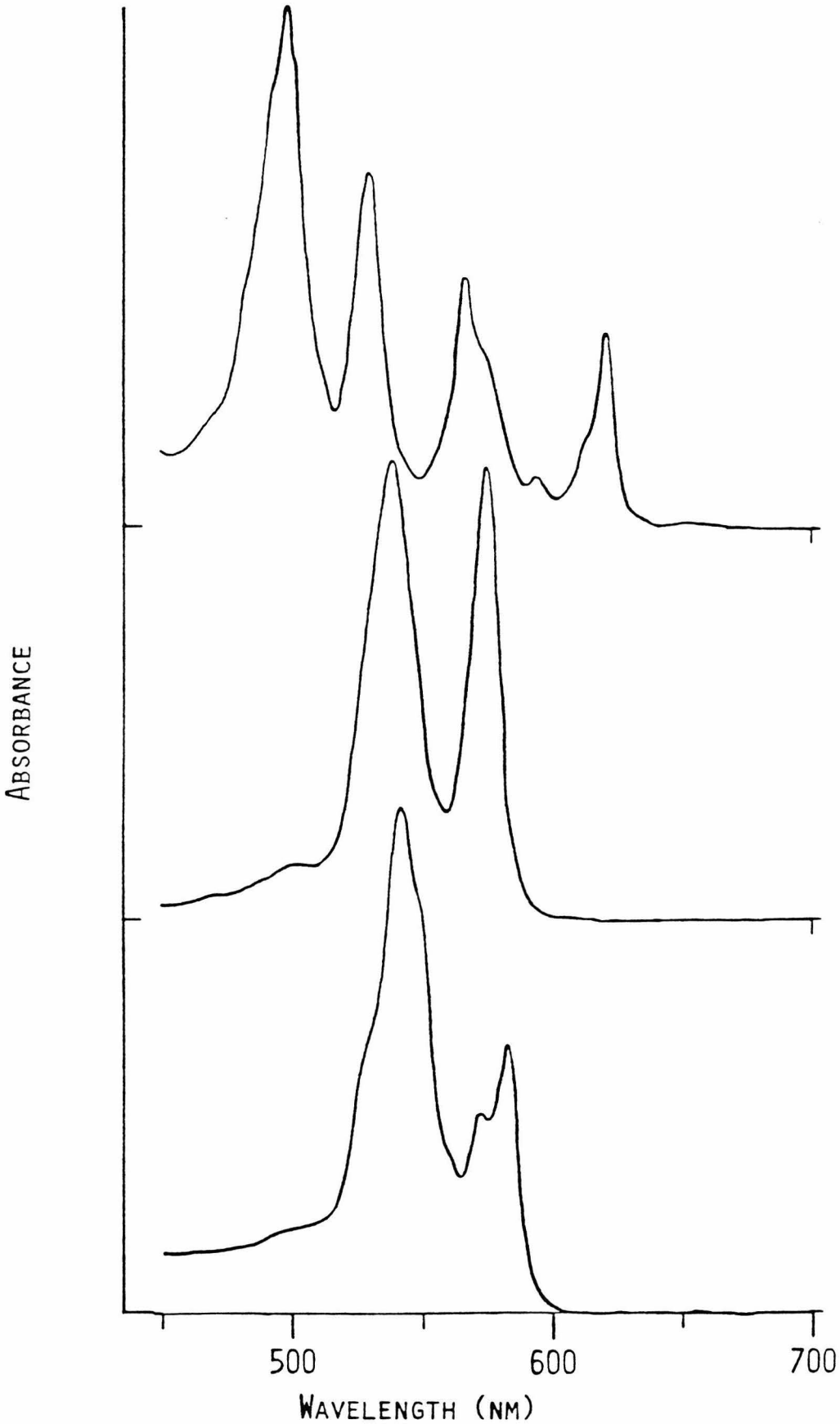
ABSORBANCE
500
600
700
WAVELENGTH (NM)

85:13.5:1.5 (v/v/v) toluene/ethyl acetate/methanol solvent system was used as the developer.[40] Progress of the chromatography was followed by sample luminescence under UV light. The zinc-mesoporphyrin IX diacid was stored in a foil-wrapped vial at -60°C.

Preparation of apomyoglobin:

The heme was removed from the myoglobin by the acidic 2-butanone extraction method.[41,42] All solutions were cooled in an ice/water bath. 20 mg of salt-free myoglobin (10 mL of 0.11 mM metMb) were acidified to pH 2.9 with 0.1 N hydrochloric acid. 2-Butanone was added in equal volume to the protein solution, and gently inverted twice to assure adequate mixing. The sample was centrifuged for five minutes to accelerate the separation of the organic and aqueous layers. The organic layer was removed and the extraction procedure was repeated two or three times. On the final extraction, the aqueous apoprotein solution was removed and transferred to a Spectrapor dialysis bag (Spectrum Medical Industries, 20.4 mm diameter, 6-8000 molecular weight cutoff, 3.2 mL/cm) that had been previously cleaned by standard methods.[43]

The sample was twice dialyzed against 1 L of 10 mM sodium bicarbonate (3.36 g $NaHCO_3$ in 4 L H_2O) followed by three times against 1 L of μ = 0.1 M phosphate buffer, pH 7.0. Each dialysis was continued for six to twelve hours. The concentration of the apoprotein was determined from the absorption spectrum (ε_{280} = 15.8 $mM^{-1}cm^{-1}$).[44] A minor peak at 424 nm indicated the incomplete removal of the iron porphyrin. Typically, heme removal in excess of 99% was achieved.

Apoprotein prepared in this fashion was immediately used for reconstitution with the zinc mesoporphyrin.

Preparation of reconstituted myoglobin:[4,5]

The apoprotein solution was maintained at 4°C or ice bath temperatures for the duration of the insertion process. Approximately 3 mg of zinc mesoporphyrin IX diacid were dissolved in 10 drops of 0.1 N NaOH(aq) in a 5 mL beaker. 2 mL of phosphate buffer (μ = 0.1 M, pH 7.0) were added to the porphyrin solution. The resulting solution was added dropwise to the apoprotein with gentle swirling. The mixture was stirred in the dark at 4°C for twelve hours. A second insertion was then made. After twelve more hours, the solution was left undisturbed overnight. The sample was centrifuged for one to two hours and the supernatant was decanted and saved for purification.

Purification of reconstituted myoglobins:

The zinc-mesoporphyrin IX reconstituted myoglobin was applied to a Sephadex G-25-80 column, equilibrated with phosphate buffer (μ = 0.01 M, pH 7.0), and eluted with the same buffer at 4°C. The protein band was collected and concentrated by Amicon ultrafiltration for loading on the phosphate (μ = 0.01 M) equilibrated CM-52 column (3 cm x 22 cm). An ionic strength gradient, μ = 0.01 to 0.1 M, was used to elute the sample at 30 mL/h. A two-flask reservoir with 1 L of μ = 0.01 M and 1 L of μ = 0.1 M phosphate buffer was used to generate the gradient. Unmodified zinc myoglobin typically required 30 - 36 h to elute, and 72 - 84 h were required for the ruthenated derivatives.

Additional μ = 0.1 M buffer was needed to complete some elutions. Zinc-substituted myoglobins were refrigerated in foil-wrapped vials and used as quickly as possible.

Instrumentation and Methods:

Emission spectra were recorded with an emission spectrophotometer described previously.[46] Samples (μ = 0.1 M, phosphate buffer pH 7.0, $A_{414} \cong 1.0$) were degassed in a vacuum cell with a 1 cm fluorescence cuvette side-arm. Spectra were recorded at ambient temperature. Excitation of the sample was by a 200 W HgXe lamp (Oriel) with a Oriel model 6240 Arc Lamp Power Supply at 404 nm (interference filter). Excitation was cut off at 446 nm and the monochromator slits were 1.0 mm.

Emission lifetime measurements of the Mb(ZnP)'s were made with a pulsed laser system described previously.[30] Excitation was at 532 nm (50 mJ/pulse at 10 Hz with 63 J/pulse lamps) with a repetition rate of 1 Hz. Fluorescence emissions were monitored through a Corning 3-67 filter at 583 and 635 nm with monochromator slits of 0.4 mm. The output signal from a Hamamatsu model R 955 photomultiplier tube was amplified by a LeCroy model VV101ATB high-speed wideband pulse amplifier. 200 pulses were collected and averaged on a Digital model PDP11/03-L computer. Data were analyzed by executing a least squares first-order fitting routine.

Transient absorption lifetime measurements of the Mb(ZnP)'s employed the same excitation and detection apparatus as the emission lifetime instrumentation except where noted. Samples (μ = 0.1 M,

phosphate buffer pH 7.0, $A_{414} \cong 1.25$) were degassed in a vacuum cell with a 1 cm fluorescence cuvette side-arm. A 500 W continuous wave tungsten lamp with an Infrared Industries Model 518 Lamp Power Supply served as the probe beam source. The beam was collimated (f = 17.7 cm, diam. = 7.5 cm) in the lamp housing and focused by a lens (f = 15.2 cm, diam. = 10.0 cm) through a series of Corning filters, 0-52, 0-51, 5-57, and 5-58. The beam was cropped by a 0.8 cm aperature and passed through the sample cell. The beam was refocused (f = 7.0 cm, diam. = 3.8 cm) onto the slit of the monochromator (0.8 mm) through a Corning 5-57 filter. A Tektronix FET probe amplifier with a 5 kΩ resistor was used for all transients except the a_5Ru(His-48)Mb(ZnP) system, in which case the LeCroy amplifier was used. The Biomation 6500 digital waveform recorder was set at 100 μs/pt for all zinc-substituted derivatives except the His-48 modification. The latter required a 100 ns/pt timebase. 40 pulses were taken at 1 Hz and the data were averaged on the PDP computer. Data were analyzed with nonlinear least squares routines. Both monophasic and biphasic first-order fits with zero and nonzero endpoints were made. Residuals were evaluated.

Computer modelling studies to evaluate the intraprotein electron-transfer distances in the ruthenated myoglobins were performed using PCMODEL.[47] Protein crystallographic data were obtained from the Brookhaven database.[48,49] Ruthenium pentaammine coordinates were evaluated from crystallographic data for ruthenium hexaammine.[50] The coordinates relative to the Brookhaven data were calculated as described in Appendix A. Three assumptions as to the ruthenium's

spatial relation to the imidazole ring were made. First, that the ruthenium was attached to N_ε, the distal nitrogen in the imidazole ring (Figure 4). Second, that the ruthenium lies in the plane defined by the imidazole ring. And third, that the N_ε-Ru vector bisects the reflex angle defined by C_δ-N_ε-C_ε. The distance was evaluated by manually rotating the imidazole side chain residue about the C_α-C_β bond. The allowable rotation was limited by nonbonded repulsive interactions with atoms at the protein surface. These interactions occurred at distances estimated from van der Waals contact radii.

Figure 4. Computer-generated structure of a_5Ru(His) from His-48 crystallographic data and calculated a_5Ru coordinates.

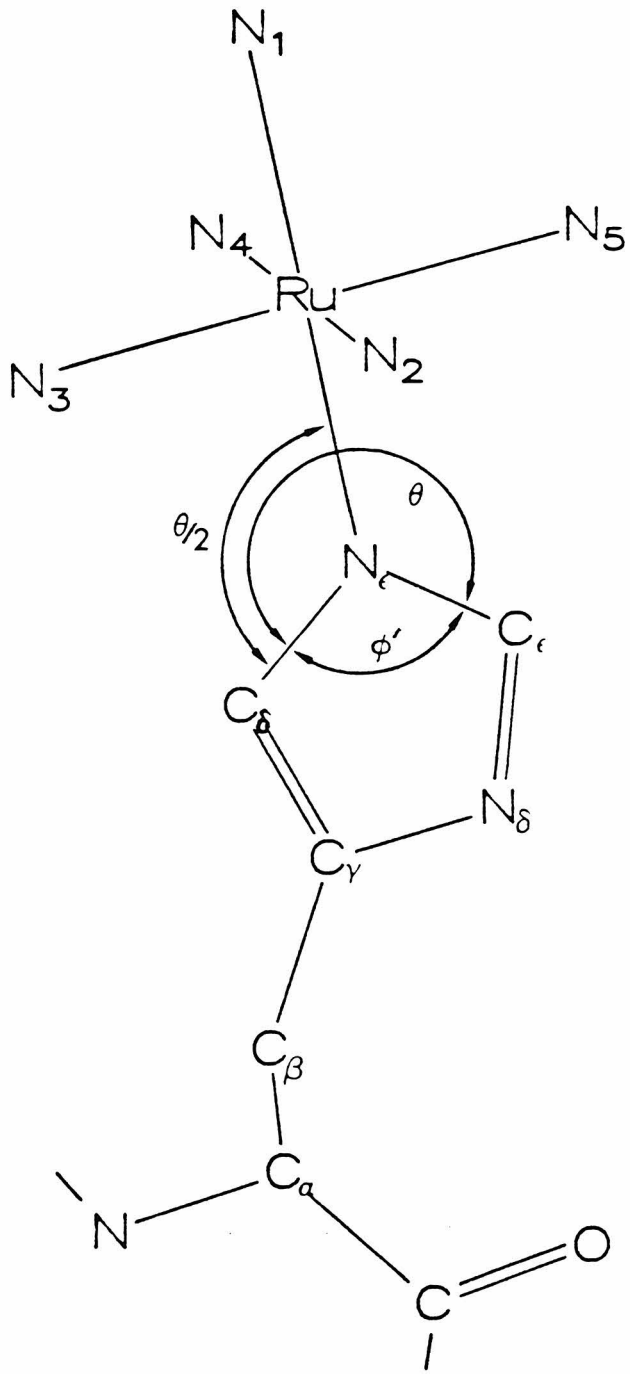
N1
N4
N5
Ru
N2
N3
θ
θ/2
Nε
φ'
Cε
Cδ
Nδ
Cγ
Cβ
Cα
N
C
O

CHAPTER III

Results and Discussion

Reconstitution:

Analytical isoelectric focusing was used to determine the purity of the a_5Ru(His)Mb(ZnP)'s following final purification.[51] The isoelectric point (pI) of Mb(ZnP) is the same as the pI of ferromyoglobin (pI = 7.4), as expected since the charge on each of these metals is 2+. Apomyoglobin is readily resolved from the reconstituted protein, because its pI is between ~8 and 9 under these experimental conditions. The broad pI band indicates that the apomyoglobin consists of multiple components, probably a result of degradation of the the less stable apoprotein. The a_5Ru(His)Mb(ZnP) samples exhibit pI's that correspond to reduced a_5Ru(His)Mb(Fe^{2+}) derivatives.

Apomyoglobin was reconstituted with zinc mesoporphyrin IX diacid with yields in excess of 90% based on protein recovery. The determination of Mb(ZnP) concentrations assumes that the A_{280} extinction coefficients for apomyoglobin and Mb(ZnP) are similar. This assumption is supported by experimental results that correlate the amount of protein present before and after reconstitutuion with the UV-visible absorption data.[52] The relative ratios of absorption maxima to the 280 nm peak provide the extinction coefficients at the other wavelengths. In particular, $A_{414}/A_{280} \cong 16$, so $\varepsilon_{414} \cong 250\ mM^{-1}\,cm^{-1}$. A comparison of the spectral data for metMb, apoMb, and Mb(ZnP) is presented in Table 1.

Emission Spectroscopy:

Emission spectra of the Mb(ZnP) are characterized by an intense,

Table 1. Comparison of absorption data for metMb, apoMb, and Mb(ZnP).

Protein	UV		Soret		α		β		ref
	λ[a]	ε[b]	λ	ε	λ	ε	λ	ε	
metMb	280	31.2	409	157	505	9.47	635	3.55	54,55
apoMb	280	15.8							44
Mb(ZnP)	280	15.8	414	250	541	11.7	583	6.1	c

a. λ (nm)

b. ε ($mM^{-1} cm^{-1}$)

c. this work

complex	absorption bands				ref
	λ[a]	ε[b]	λ	ε	
$a_5Ru(His)^{3+}$	303	2.1	450	0.29	56
$a_5Ru(His)^{2+}$	260	3.26	280	3.16	56

symmetrical band at 586 nm and a weaker system composed of two broad peaks at 635 and 643 nm. No other emissions were observed in the wavelength range 550 to 800 nm.[57] These data accord with literature reports of fluorescence from Mb(ZnP)[58] and the emission properties of zinc-substituted hemoglobins.[45] Singlet emission lifetimes were not resolved with the nanosecond laser system (8 ns FWHM pulse), implying an upper limit of 10 ns for these lifetimes. Singlet lifetimes of other zinc porphyrins in aqueous solution have been reported to be on the order of 1 - 3 ns.[59] Zinc triplet emission has been observed in myoglobin at low temperature[60] and in other metalloproteins,[61] but room temperature solutions of Mb(ZnP) do not display phosphorescence.

Kinetics:

Transient flash kinetic methods have been used to study the electron-transfer quenching in zinc/ruthenium-modified myoglobins. A kinetic analysis of the mechanism proposed in Scheme 1 for the a_5Ru(His)Mb(ZnP) system is presented in Appendix B. The electron-transfer rates were determined by observing the quenching of the $^3ZnP^*$ decay. The rate expression derived (Equation 1) consists of two first-order components, one containing the intrinsic decay, k_d, and forward, k_f, electron-transfer rate constants and the other containing the reverse rate, k_b,

$$[a_5Ru(His)Mb(ZnP)]_t = A_o[1 + K_1 \exp(-(k_d + k_f)t) + K_2 \exp(-k_b t)] \qquad (1)$$

where $A_o = [a_5Ru(His)Mb(^3ZnP^*)]$ at $t = 0$ s and K_1 and K_2 are preex-

ponentials as given in Appendix B. In addition to electron-transfer quenching, as shown in Scheme 1, the possibility of $^3ZnP^*$ deactivation by Förster energy transfer was considered. The rate of Förster or dipole-dipole energy transfer can be calculated using the equation[62]

$$k = [9(\ln 10)\kappa^2/128\pi^5 N_A n^4 \tau R^6] \int F_D(\lambda)\varepsilon_A(\lambda)\lambda^4 d\lambda. \quad (2)$$

In the case of $a_5Ru(His)Mb(ZnP)$, the most important term in the equation is the overlap integral, $\int F_D(\lambda)\varepsilon_A(\lambda)\lambda^4 d\lambda$. This integral represents the extent of overlap between the $^3ZnP^*$ emission and ruthenium absorption spectra. This mechanism of energy transfer populates the lowest-lying ruthenium energy level, $^4T_{1g}$. The overall interaction, while spin allowed, involves two spin forbidden transitions, $^3ZnP^* \rightarrow {}^1ZnP$ (14300 cm^{-1})[60] and $^2Ru \rightarrow {}^4Ru$ (16700 cm^{-1}).[63] Overlap between the $^3ZnP^*$ emission and the ^2Ru absorption is negligible, and therefore Förster energy transfer should not make a significant contribution to the quenching rate. Other energy transfer mechanisms, for example dipole-quadrupole and electric dipole/magnetic dipole, are expected to contribute even less than the dipole-dipole interaction.[64]

Electron-transfer quenching, as described in Scheme 1, is assumed to be the dominant deactivation pathway for the $a_5Ru(His)Mb(^3ZnP^*)$ system.[65] Preliminary results from bimolecular electron transfer studies support the conclusion that the dominant mechanism of triplet quenching is by electron transfer; the reaction between zinc-substituted cytochrome *c* (horse heart) and a_6Ru^{3+} indicates that energy transfer accounts for less than 0.01% of the total triplet quench-

ing.[66a]

Under pulsed laser experimental conditions, the a_5Ru(His)Mb(ZnP) samples are quite stable. The absorption spectra remain unchanged (<1%) even after 500 laser pulses. A slow reversible decay amounting to about 10% of the transient optical density change was observed. The contribution of this slow component was minimized by using high purity samples.[67] The minor component has been attributed to protein impurities in similar investigations of zinc-substituted, ruthenium-modified cytochrome *c*.[66b] Regardless, the initial optical density is restored within one second of the excitation pulse (8 ns FWHM, 1 Hz repetition). In contrast, when using a broad band microsecond excitation source, the sample undergoes significant decomposition (~50%) within five flashes.

The native Mb(ZnP) data fit a monophasic first-order nonzero endpoint expression for at least four half-lives (Figures 5 and 6). The rate constant determined by this fit, 40 ± 2 s^{-1}, corresponds to the intrinsic triplet decay rate, k_d. All rate constants are reported at 25°C unless otherwise indicated. The decay rate of Mb(^{3}ZnP*) (Table 2) ranges from 38 ± 5 s^{-1} (7.6°C) to 42 ± 1 s^{-1} (38.6°C), indicating that within experimental error, there is no temperature dependence. Values of k_d determined over a concentration range of 3 μM (A_{414} = 0.75) to 90 μM (A_{414} = 2.37, b = 0.1 cm) are 41 ± 2 s^{-1} and 46 ± 4 s^{-1}, respectively, implying that no bimolecular quenching of the triplet zinc excited state occurs. In addition, when Mb(ZnP) was reduced with sodium dithionite,[68] k_d remains unchanged (39 ± 3 s^{-1}), demonstrating that oxidized protein and/or porphyrin impurites do not

Figure 5. Transient absorption data for Mb(^{3}ZnP*).

Figure 6. Analysis (fit and residuals) of Mb(^{3}ZnP*) data (monophasic first-order nonzero endpoint).

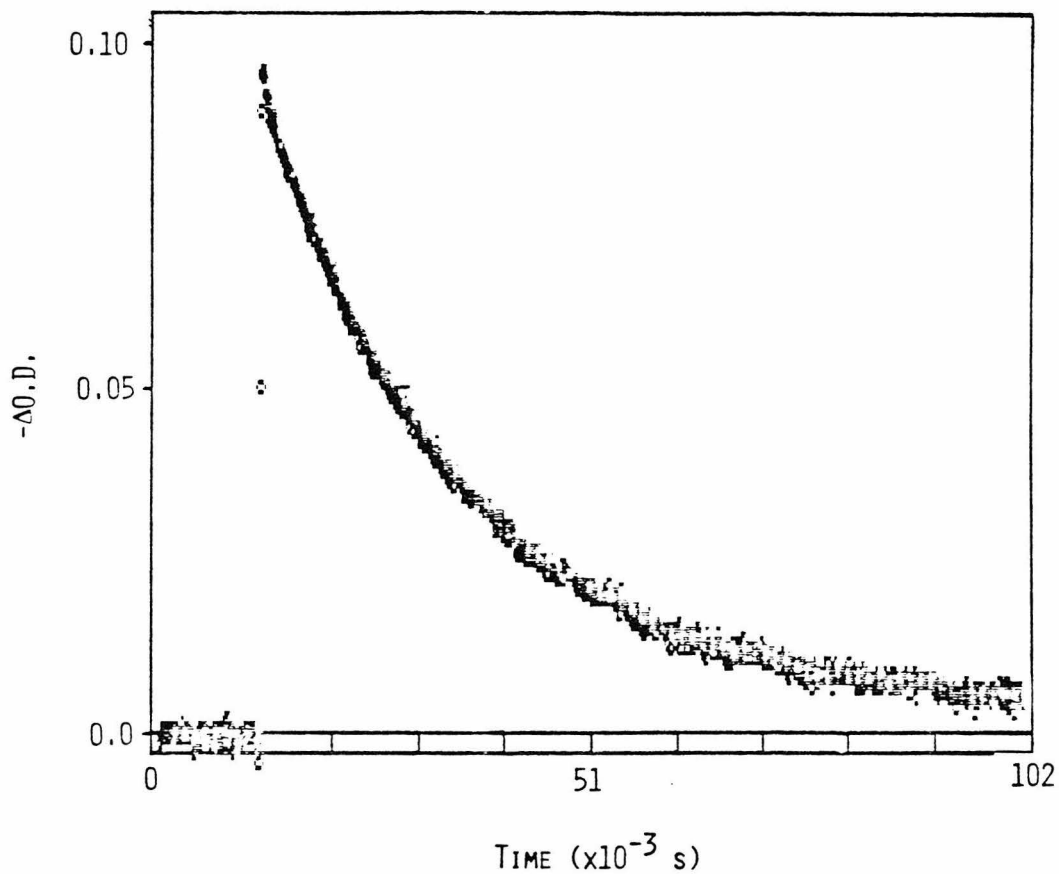
0.10
0.05
0.0
-ΔO.D.
0
51
102
TIME (x10^{-3} s)

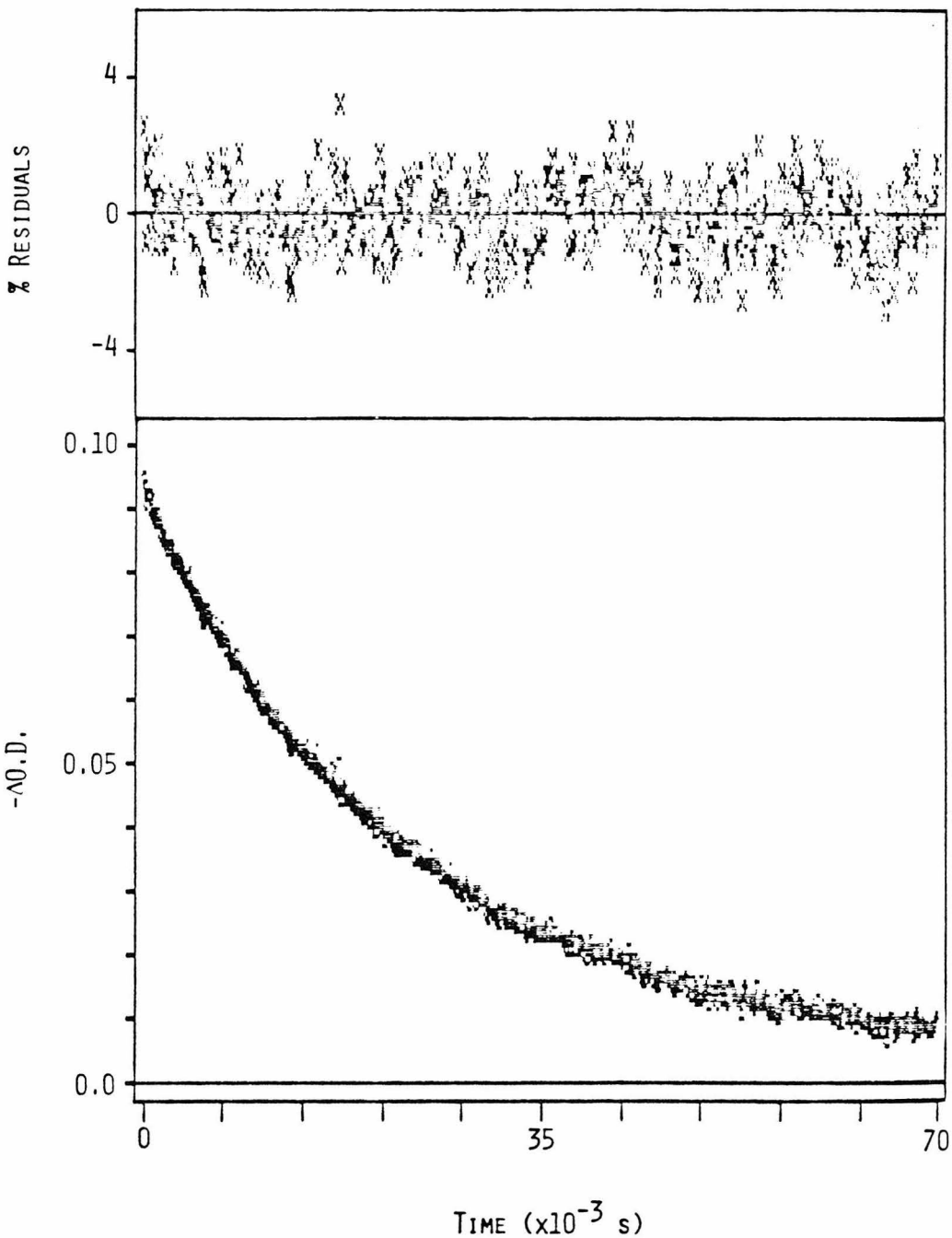
% RESIDUALS
4
0
-4
-ΔO.D.
0.10
0.05
0.0
0
35
70
TIME (x10^{-3} s)

Table 2. Rate constants for Mb(ZnP) and a_5Ru(His-48)Mb(ZnP).

Temp.	Mb(ZnP)		a_5Ru(His-48)Mb(ZnP)	
°C	$k_{obs}(=k_d)x10^{-1}$		$k_{obs}(=k_f)x10^{-4}$	
(± 0.1)	(s^{-1})	$\ln(k_d/T)$	(s^{-1})	$\ln(k_f/T)$
7.6	3.8± 0.5	-2.00± 0.13	5.4± 0.9	5.26± 0.16
11.8	3.9± 0.4	-1.99± 0.11	6.2± 0.8	5.38± 0.13
16.2	3.9± 0.3	-2.00± 0.08	6.2± 0.6	5.37± 0.10
20.6	4.0± 0.3	-1.99± 0.07	6.3± 1.3	5.37± 0.18
25.0	4.0± 0.2	-2.01± 0.05	7.0± 0.8	5.46± 0.10
29.4	4.1± 0.2	-2.00± 0.05	7.7± 1.4	5.54± 0.19
34.0	4.2± 0.2	-1.99± 0.04	8.0± 1.0	5.56± 0.12
38.6	4.2± 0.1	-2.00± 0.03	8.1± 1.4	5.56± 0.19

significantly quench $^3ZnP^*$.

The a_5Ru(His-48)Mb(ZnP) data also fit a monophasic first-order nonzero endpoint expression for at least four half-lives (Figures 7 and 8). A rate constant of 7.0 ± 0.8 x 10^4 s^{-1} was obtained. Subtraction of the intrinsic decay rate (40 ± 2 s^{-1}) does not affect this result, hence $k_{obs} \equiv k_f$. The a_5Ru(His-48)Mb($^3ZnP^*$) quenching rate constant exhibits a slight temperature dependence (Table 2), ranging from 5.4 ± 0.9 x 10^4 s^{-1} (7.6°C) to 8.1 ± 1.4 x 10^4 s^{-1} (38.6°C). The decay of the photoexcited a_5Ru(His-48)Mb(ZnP) was also measured following dithionite reduction of the a_5Ru(His)$^{3+}$ acceptor. The observed decay rate, 50 ± 5 s^{-1}, is similar to the intrinsic native decay rate, k_d.

The residuals corresponding to a monophasic first order nonzero endpoint fit of the a_5Ru(His-81)Mb(ZnP) data indicate severe deviations from monophasic behavior (Figures 9 and 10). These data can be satisfactorily fit to a biphasic first order zero endpoint expression (Figure 11). Nine half-lives of the fast component were used in the analysis. The observed rate, 126 ± 12 s^{-1}, corresponds to a k_f of 86 ± 12 s^{-1}. The second component contributes less than 10% to the transient absorption measurement and was observed for less than two half-lives. Similar analyses of the a_5Ru(His-116)Mb(ZnP) and a_5Ru(His-12)Mb(ZnP) data yielded electron-transfer rate constants, k_f, of 89 ± 3 s^{-1} and 101 ± 11 s^{-1}, respectively. The His-81, 116, and 12 derivatives exhibit moderate temperature dependences over the range 5 - 40°C (Table 3). Over the concentration range 3 - 15 μM a_5Ru(His-81)Mb(ZnP) showed no variation in k_{obs}. Following reduction of the

Figure 7. Transient absorption data for a_5Ru(His-48)Mb(^{3}ZnP*).

Figure 8. Analysis (fit and residuals) of a_5Ru(His-48)Mb(^{3}ZnP*) data (monophasic first-order nonzero endpoint).

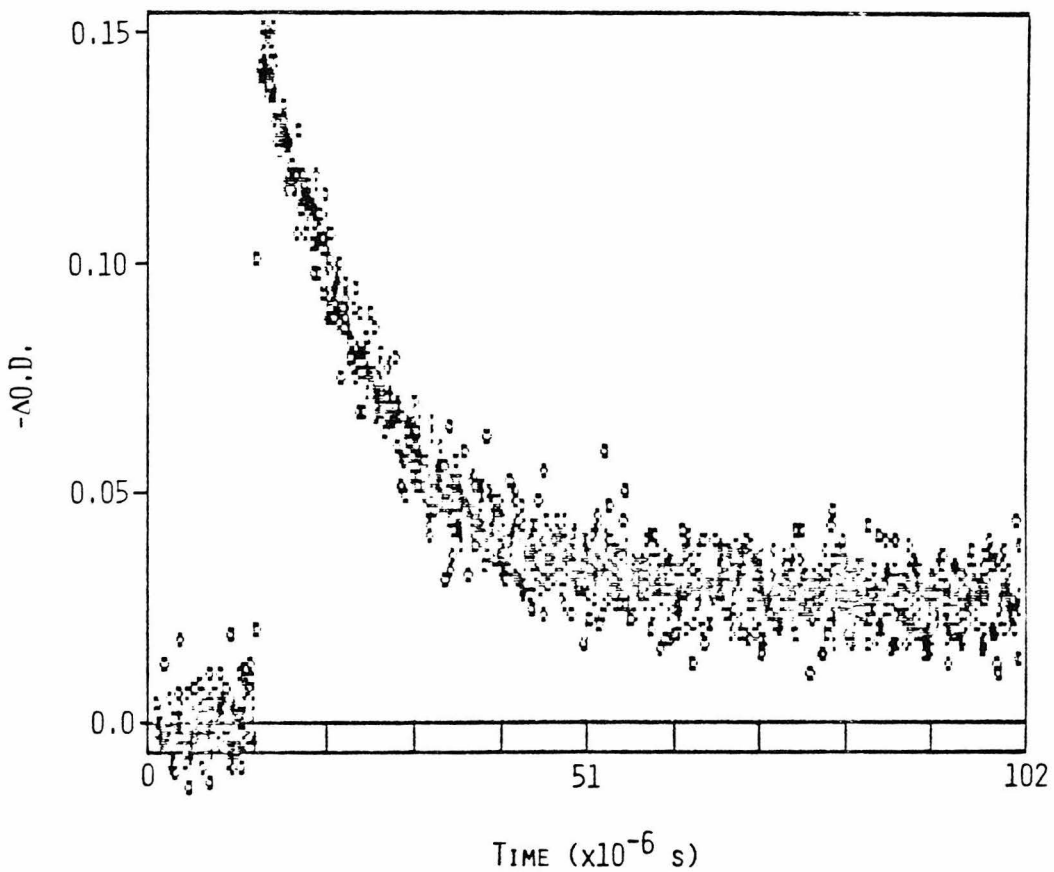
0.15
0.10
0.05
0.0
-ΔO.D.
0
51
102
TIME (x10^{-6} s)

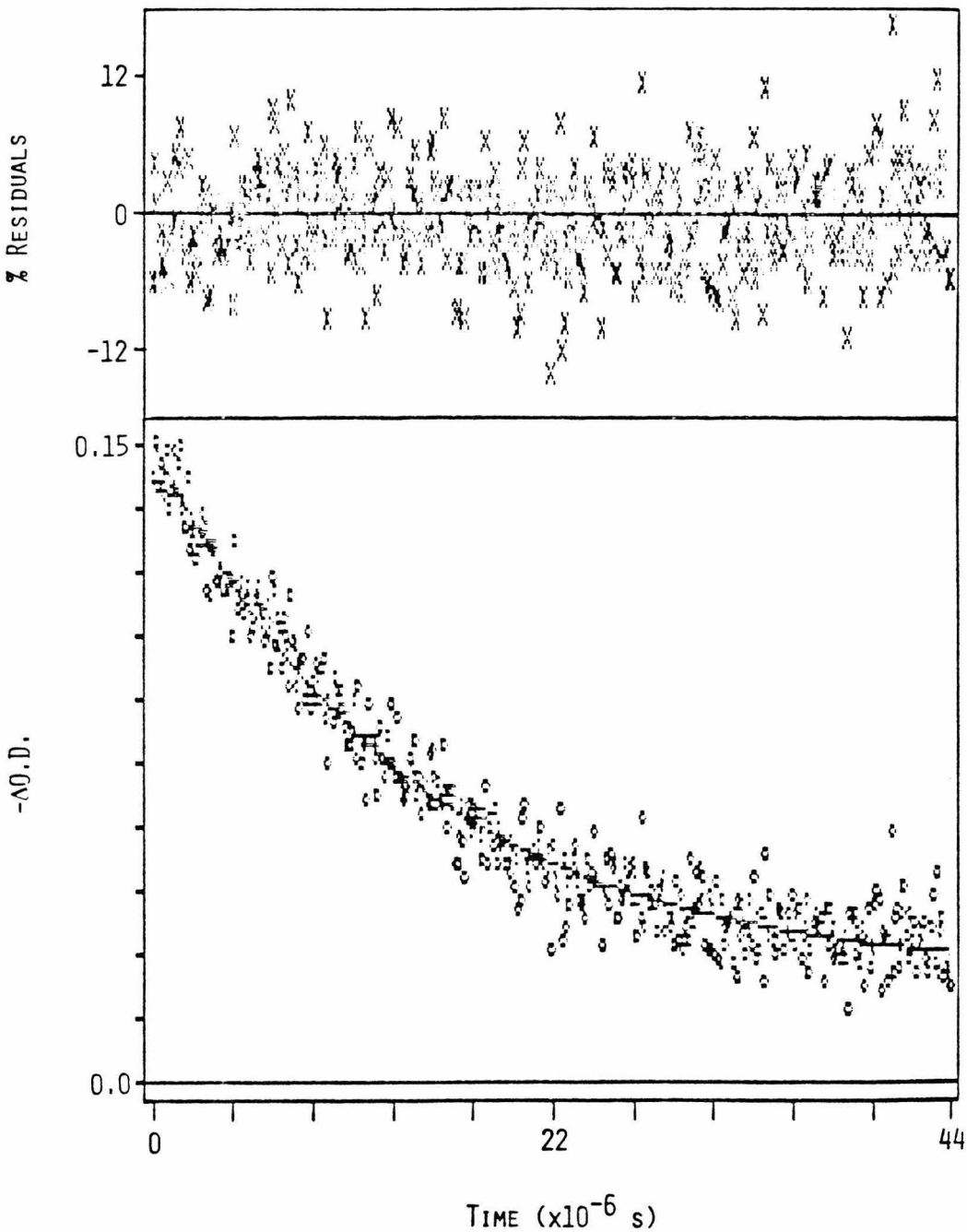
12
0
-12
% RESIDUALS
0.15
0.0
-ΔO.D.
0
22
44
TIME (x10^{-6} s)

Figure 9. Transient absorption data for a_5Ru(His-81)Mb(^{3}ZnP*).

Figure 10. Analysis (fit and residuals) of a_5Ru(His-81)Mb(^{3}ZnP*) data (monophasic first-order nonzero endpoint).

Figure 11. Analysis (fit and residuals) of a_5Ru(His-81)Mb(^{3}ZnP*) data (biphasic first-order zero endpoint).

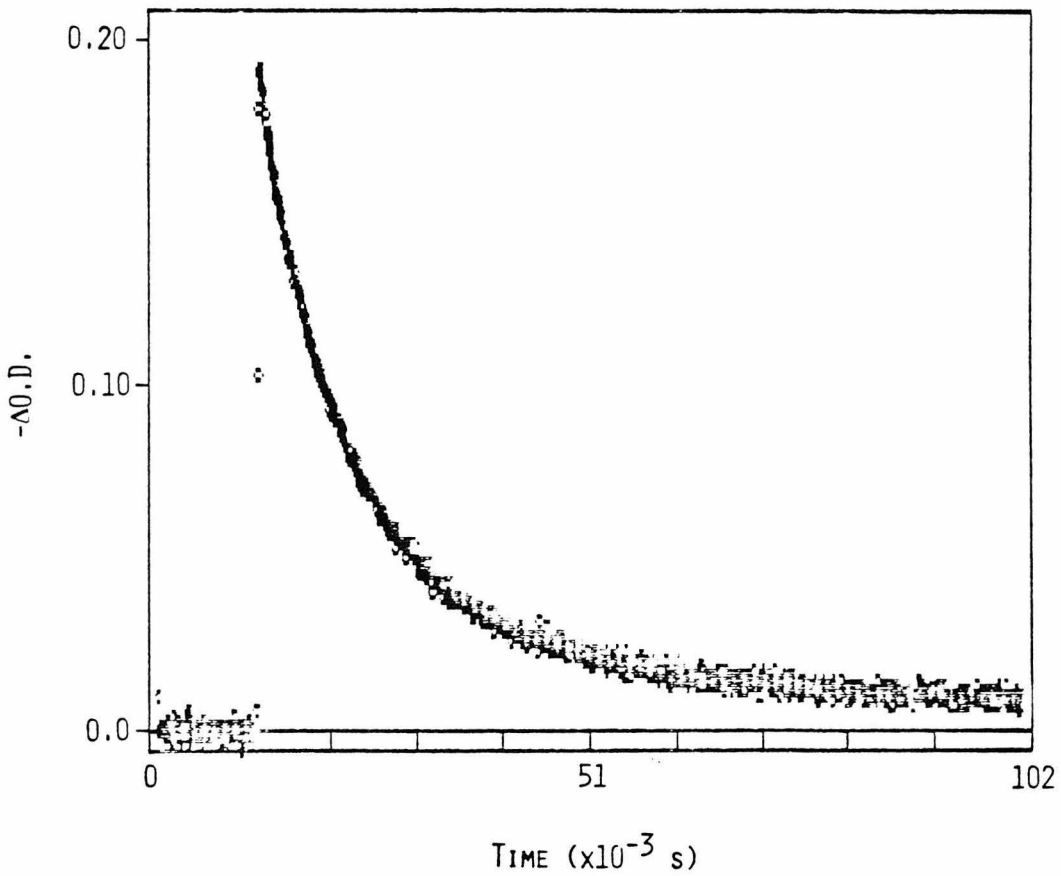
0.20
0.10
0.0
-ΔO.D.
0
51
102
TIME (x10^{-3} s)

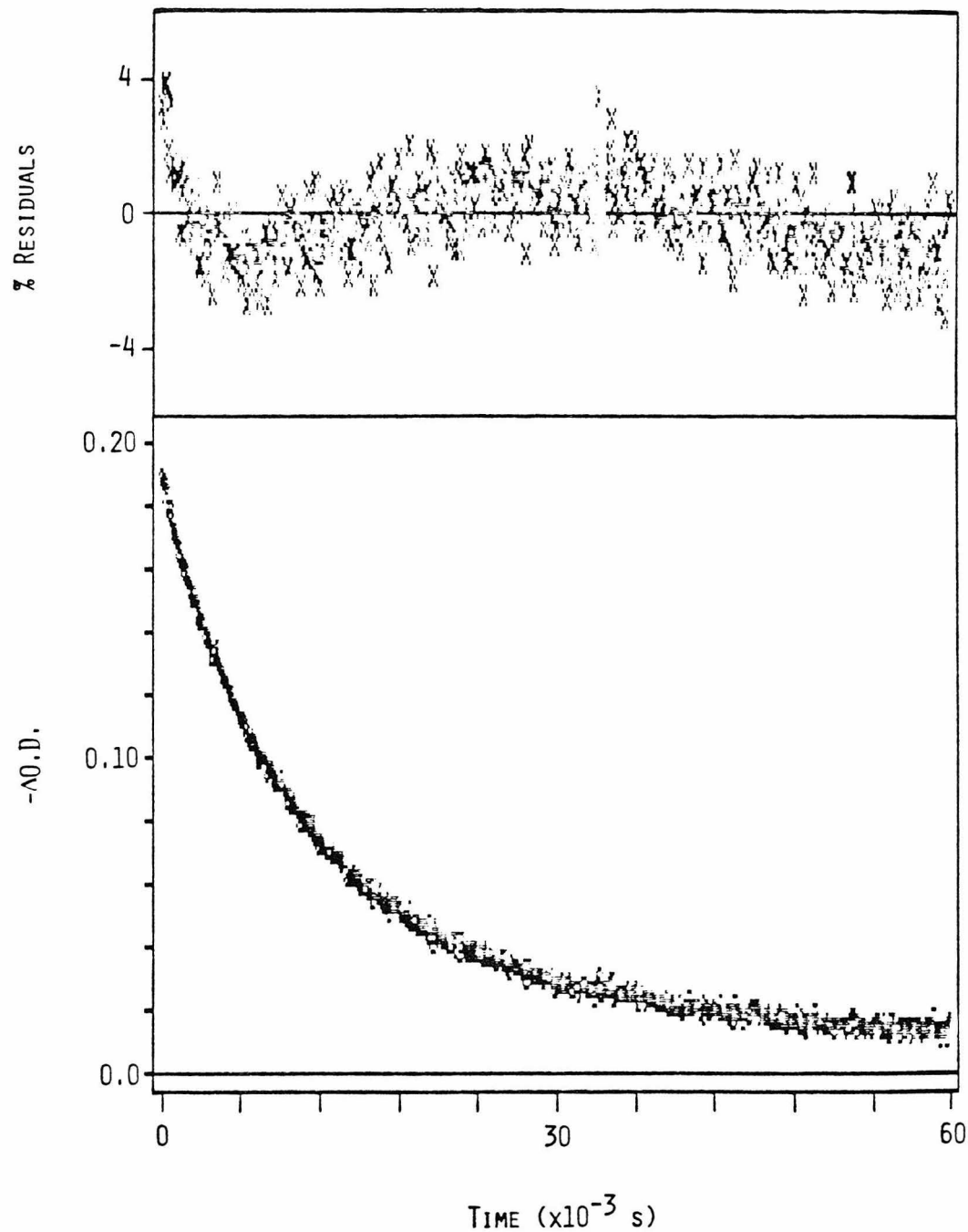
% RESIDUALS
4
0
-4
0.20
0.10
0.0
-ΔO.D.
0
30
60
TIME (x10^{-3} s)

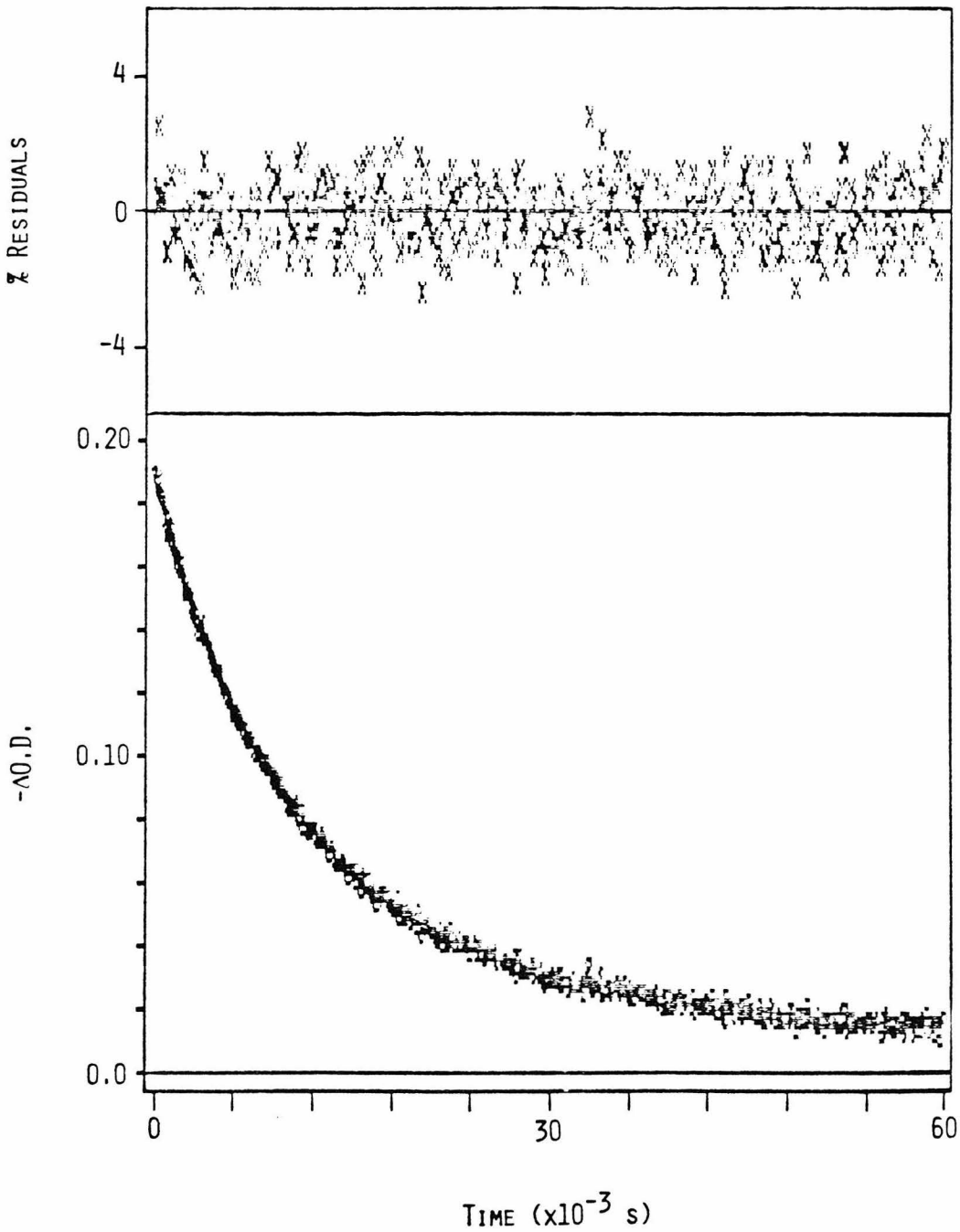
% Residuals
4
0
-4
0.20
0.10
0.0
-ΔO.D.
0
30
60
Time (x10^{-3} s)

Table 3. Rate constants for a_5Ru(His)Mb(ZnP), His-81, 116, and 12.

	a_5Ru(His)Mb(ZnP)					
Temp.	His-81		His-116		His-12	
°C	k_{obs}[a]	k_f[b]	k_{obs}[a]	k_f[b]	k_{obs}[a]	k_f[b]
(± 0.1)	(s^{-1})	(s^{-1})	(s^{-1})	(s^{-1})	(s^{-1})	(s^{-1})
7.6	7.4± 0.2	3.6± 0.5	8.6± 0.6	4.8± 0.8	9.9± 0.7	6.1± 0.9
11.8	9.0± 1.3	5.1± 1.4	9.2± 0.4	5.4± 0.6	10.3± 0.3	6.4± 0.5
16.2	9.7± 0.8	5.8± 0.9	10.5± 0.2	6.6± 0.4	11.7± 0.3	7.8± 0.4
20.6	11.2± 1.0	7.3± 1.0	11.4± 1.2	7.5± 1.2	11.9± 1.6	8.0± 1.6
25.0	12.6± 1.2	8.6± 1.2	13.0± 0.2	8.9± 0.3	14.1± 1.1	10.1± 1.1
29.4	13.8± 0.5	9.7± 0.5	14.4± 0.7	10.3± 0.7	15.7± 1.9	11.6± 1.9
34.0	15.2± 2.2	11.0± 2.2	15.9± 0.1	11.7± 0.2	17.4± 0.5	13.3± 0.5
38.6	17.2± 2.1	13.0± 2.1	18.3± 2.2	14.1± 2.2	19.2± 1.7	15.0± 1.7

a. $k_{obs} \times 10^{-1}$

b. $k_f \times 10^{-1}$

a_5Ru(His-81)Mb(ZnP) sample, the observed rate, 45 ± 4 s^{-1}, was found to be within experimental error of the native decay rate, k_d.

Activation Enthalpies:

The enthalpies of activation, $\Delta H^{\ddagger}$, were determined from Eyring plots ($\ln(k_f/T)$ versus 1/T). These results, compiled in Tables 2 and 4, are presented in Figures 12-16. The $\Delta H^{\ddagger}$ in Mb(ZnP) is 0.0 ± 0.9 kcal mol^{-1}. The a_5Ru(His-48)Mb(ZnP) activation enthalpy is 1.7 ± 1.6 kcal mol^{-1}. The His-81, 116, and 12 derivatives exhibit $\Delta H^{\ddagger}$'s of 5.6 ± 2.5, 5.4 ± 0.4, and 4.7 ± 0.9 kcal mol^{-1}, respectively. The activation entropies, -31 to -34 eu, are similar for all four derivatives.

The reason for two distinct activation enthalpies is not readily apparent. In considering possible protein effects on the activation enthalpies, the locations of the modified histidine residues need to be examined. His-12 (A helix), His-48 (CD-corner), His-81 (EF-corner), and His-116 (G helix)[48] all lie in different protein regions. A residue within the CD-corner (arginine-45), along with elements of the E helix (histidine-64 and valine-68), have been implicated in playing a role in the conformational changes in myoglobin that open a channel for dioxygen binding to the heme.[69] Additionally, low temperature X-ray diffraction measurements permit the assignment of isotropic atomic mean-square displacements of the nonhydrogen atoms.[70] When corrected for solvent interactions, the CD-corner exhibits the greatest mobility of any myoglobin region.[71] The location of His-48 in the flexible CD-corner may then contribute to the measured difference in activation enthalpies between the His-48 modification and the

Table 4. Eyring plot data for a_5Ru(His)Mb(ZnP), His-81, 116, and 12.

Temp.	a_5Ru(His)Mb(ZnP)		
°C	His-81	His-116	His-12
(± 0.1)	$\ln(k_f/T)$	$\ln(k_f/T)$	$\ln(k_f/T)$
7.6	-2.05± 0.13	-1.77± 0.16	-1.53± 0.13
11.8	-1.72± 0.27	-1.66± 0.10	-1.49± 0.12
16.2	-1.61± 0.15	-1.48± 0.06	-1.31± 0.06
20.6	-1.39± 0.15	-1.37± 0.16	-1.30± 0.20
25.0	-1.24± 0.26	-1.21± 0.03	-1.08± 0.11
29.4	-1.14± 0.06	-1.08± 0.07	-0.96± 0.17
34.0	-1.03± 0.20	-0.97± 0.02	-0.84± 0.04
38.6	-0.88± 0.16	-0.79± 0.15	-0.73± 0.11

Figure 12. Plot of $\ln(k_d/T)$ versus $1/T$ for Mb(^{3}ZnP*).

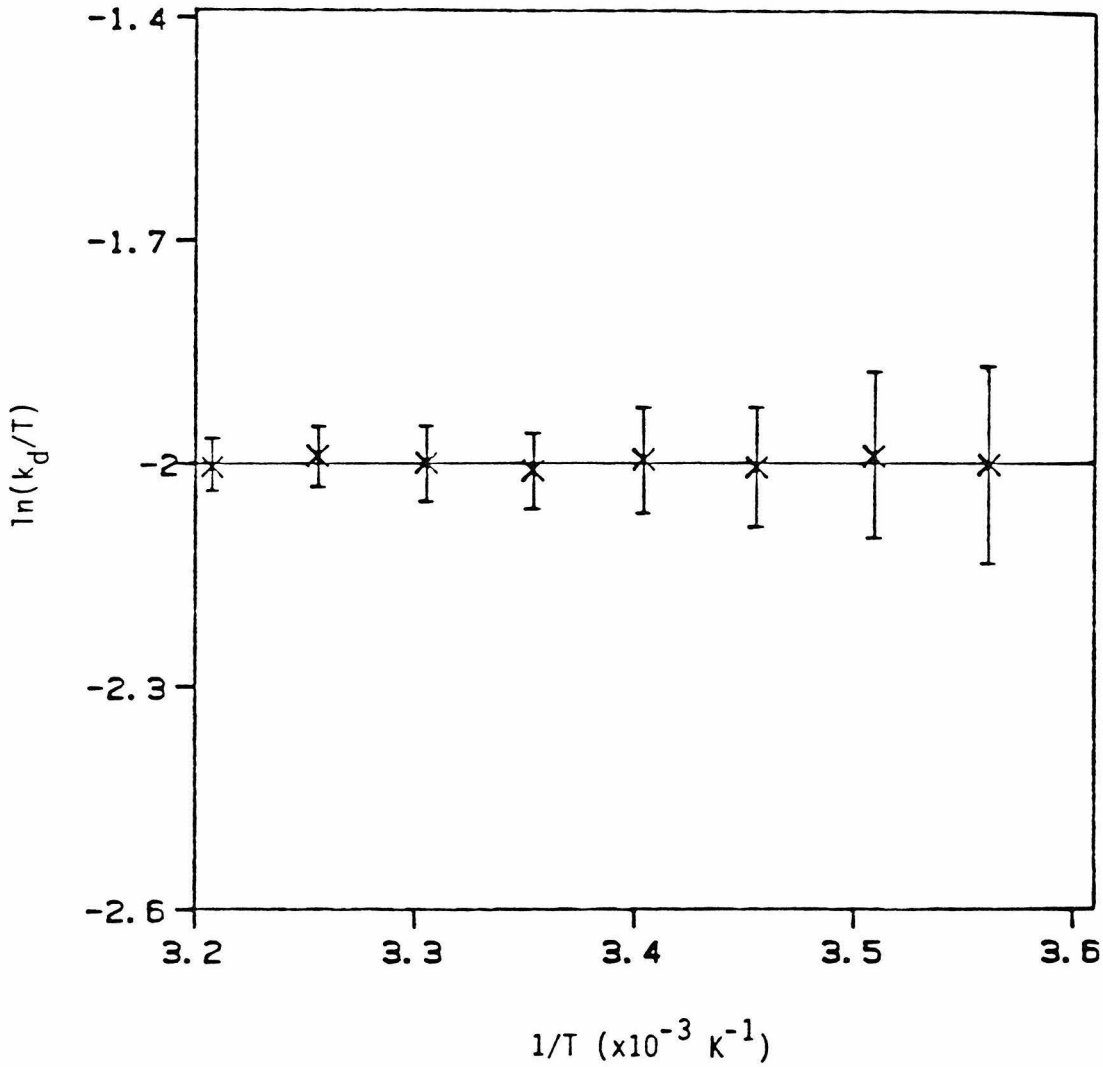
-1.4
-1.7
-2
-2.3
-2.6
3.2
3.3
3.4
3.5
3.6
ln(k_d/T)
1/T (x10^-3 K^-1)

Figure 13. Plot of $\ln(k_f/T)$ versus $1/T$ for a_5Ru(His-48)Mb(^{3}ZnP*).

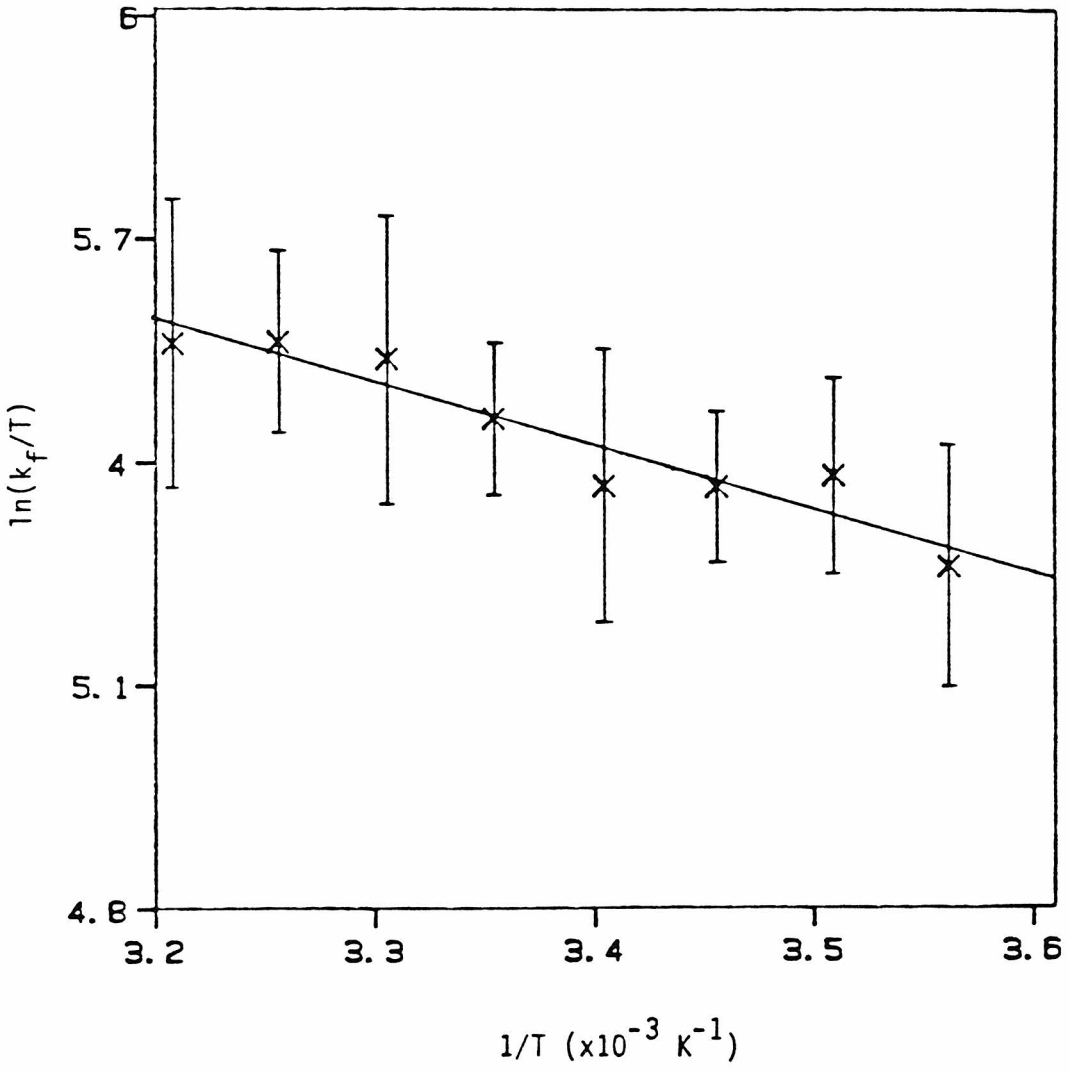
6
5.7
4
5.1
4.8
3.2
3.3
3.4
3.5
3.6
ln(k_f/T)
1/T (x10^-3 K^-1)

Figure 14. Plot of $\ln(k_f/T)$ versus $1/T$ for a_5Ru(His-81)Mb(^{3}ZnP*).

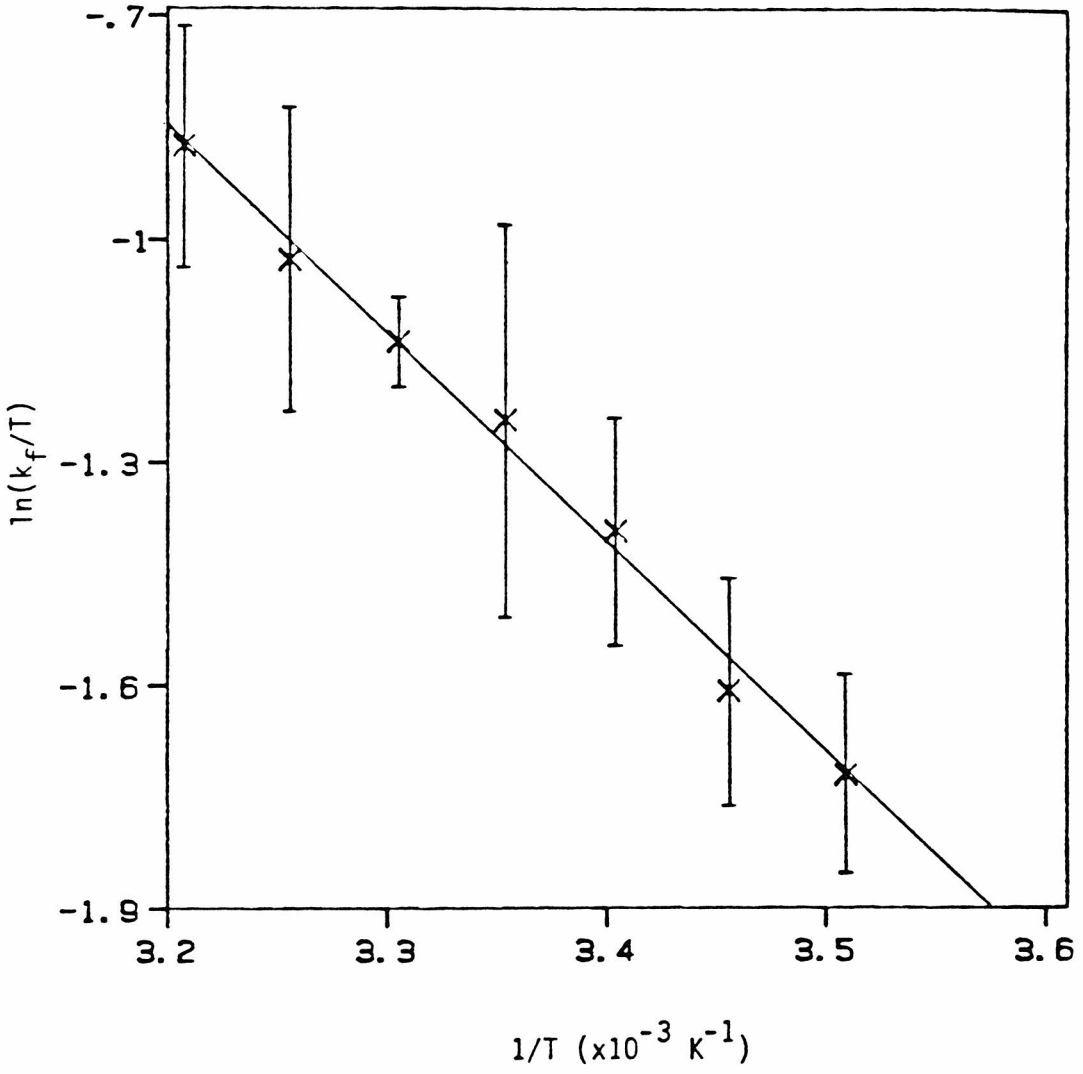
-.7
-1
-1.3
-1.6
-1.9
3.2
3.3
3.4
3.5
3.6
ln(k_f/T)
1/T (x10^-3 K^-1)

Figure 15. Plot of $\ln(k_f/T)$ versus $1/T$ for a_5Ru(His-116)Mb(^{3}ZnP*).

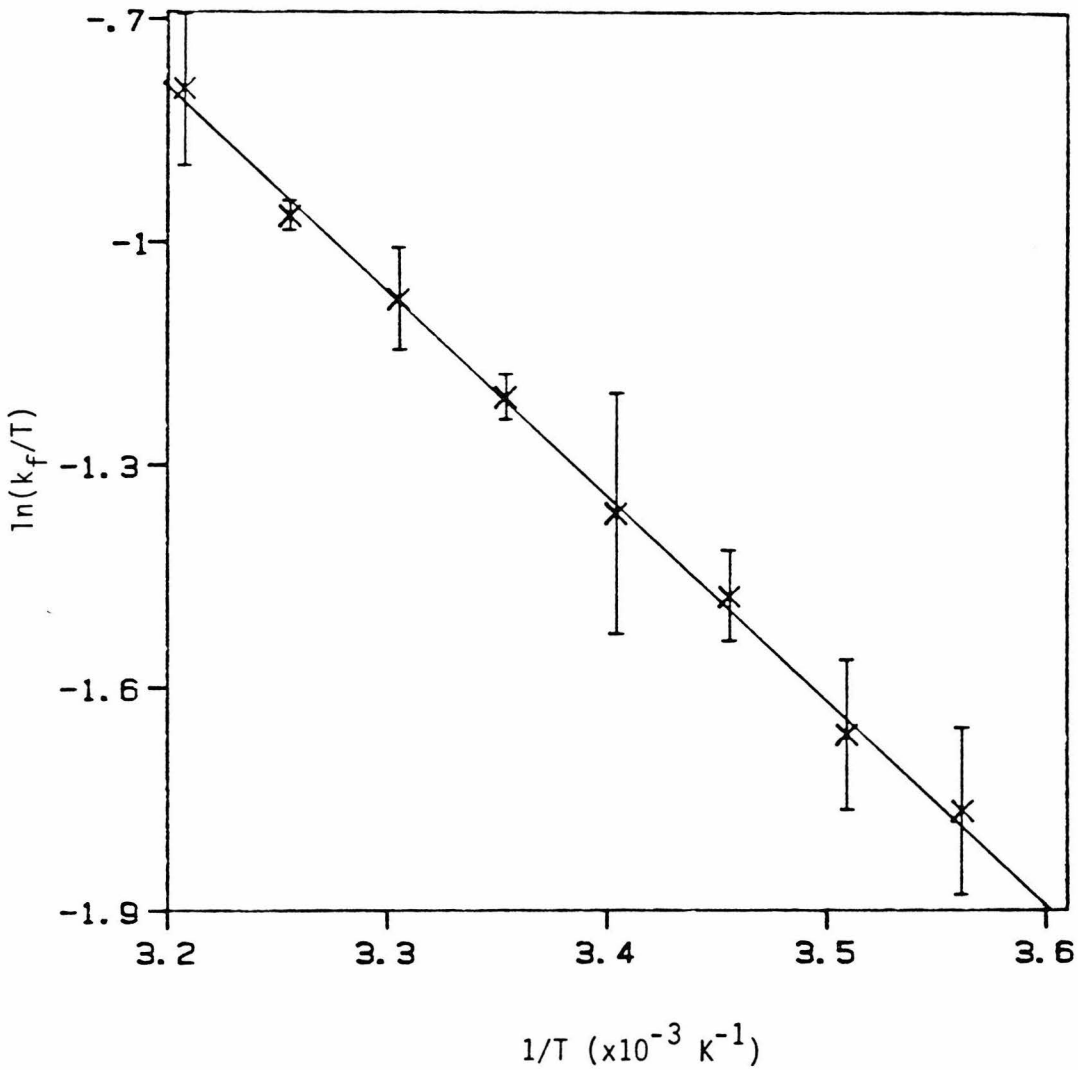
-.7
-1
-1.3
-1.6
-1.9
ln(k_f/T)
3.2
3.3
3.4
3.5
3.6
1/T (x10^-3 K^-1)

Figure 16. Plot of $\ln(k_f/T)$ versus $1/T$ for a_5Ru(His-12)Mb(^{3}ZnP*).

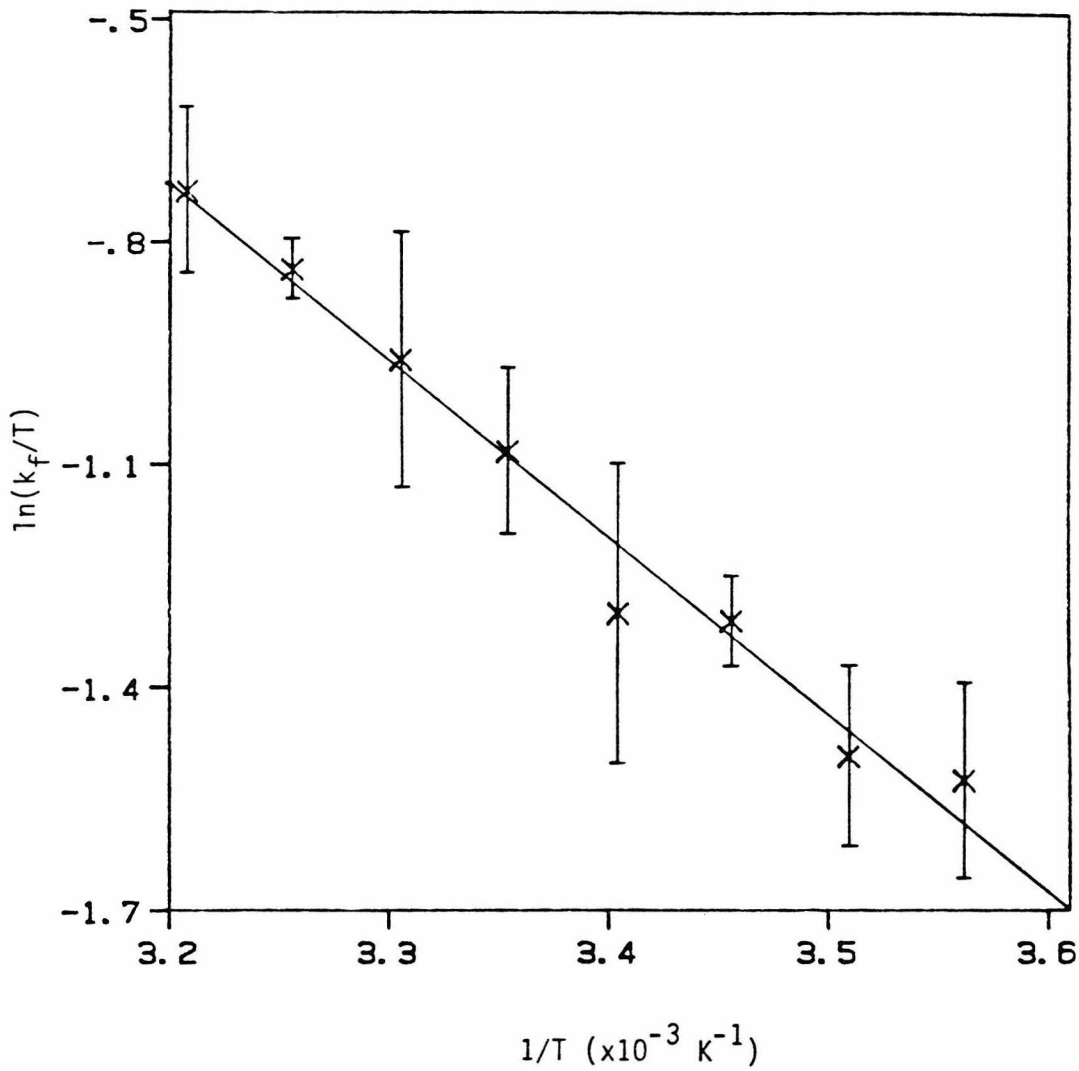
-.5
-.8
-1.1
-1.4
-1.7
ln(k_f/T)
3.2
3.3
3.4
3.5
3.6
1/T (x10^-3 K^-1)

other derivatives.

Distance Evaluation:

The determination of the distance dependence of intramolecular electron-transfer rates is essential to the understanding of electron-transfer dynamics and mechanisms. From theoretical considerations, the intersite distance is expected to have a profound effect on the extent of interaction between the electronic states of the donor and acceptor. Experimental measurements of the rate dependence on distance are necessary in order to evaluate the mechanism of electronic coupling.

Theoretical treatments of electronic coupling fall into two broad categories characterized as through-bond and through-space. Both are concerned with the decay of the donor and acceptor wavefunctions over increasing distance. In general, the electronic coupling matrix element, H_{AB}, is expected to decay exponentially with distance.

$$H_{AB} = H^{\circ}_{AB} \exp(-\alpha(R - R_o) \qquad (3)$$

where H°_{AB} is the electronic interaction at van der Waals contact, $R = R_o$.[72] Both through-bond and through-space mechanisms should lead to exponential distance dependences. The value of α, however, is expected to be lower in the through-bond case, as the wavefunction decay is expected to be affected by interactions with the bond orbitals. Some treatments predict a low power-law dependence for the through-bond transfer mechanism.[73]

Theoretical studies have shown that the through-bond and through-space pathways are distinct limits of the general mechanism of electron tunneling.[74] The limit selected is determined by the energetics of the donor, acceptor, and medium, as well as the degree of interaction between adjacent through-bond elements. Fixed-site systems have incorporated rigid linkers to separate the donor and acceptor.[15-19] A through-bond mechanism has been proposed in many of these systems. Recent theoretical results indicate that electron transfer across a hydrocarbon frame is facilitated by carbon-carbon σ-bond interactions.[20]

In order to assess the contributions of through-bond and through-space mechanisms in protein-mediated systems, the electron-transfer rates obtained in this work have been examined in the light of myoglobin structural results.

Through-bond:

The through-bond distances were measured from the proximal histidine (His-93) that serves as the axial ligand to the heme in the native protein structure. The same residue is known to coordinate the zinc porphyrin, in fact, five-coordinate zinc porphyrin is virtually isostructural with five-coordinate deoxy iron(II) porphyrins.[75] The number of intervening residues between His-93 and each of the ruthenium modification sites is presented in Table 5. The through-bond separation (in Angstroms) is based on 4.7 Å/residue.[76] No obvious correlation exists between the electron-transfer rates and their corresponding through-bond distances. It seems likely that a through-

Table 5. Through-bond distances from the axial histidine to the ruthenium modification sites in sperm whale myoglobin.

a_5Ru(His)Mb	residues (#)	distance[a] (Å)	k_f (s^{-1})	$\ln(k_f)$
His-12	81	380	101± 11	4.62± 0.11
His-48	45	210	70± 8x10^3	11.16± 0.10
His-81	12	56	86± 12	4.45± 0.26
His-116	23	110	89± 3	4.49± 0.03

a. 4.7 Å/residue

space mechanism is operative in the a_5Ru(His)Mb(ZnP) systems.

Through-space:

The through-space distance was calculated from the crystallographic data between selected atoms in the protein structure; both metal to metal (center to center) and edge to edge distances were evaluated. Typically, the porphyrin ring edge and the imidazole ring are the locations of the atoms used to determine the edge to edge distances. A minimum distance of 4 Å is incorporated into the data plots to reflect the nonbonded interactions between the porphyrin edge and inner sphere ligand that discourage any closer contact. Table 6 presents these data. A plot of $\ln(k_f)$ versus distance (R) (Figure 17) shows that the rate initially falls off with distance, but at moderately long ranges (24 - 29 Å metal to metal, 19 - 23 Å edge to edge), the electron-transfer rate appears to level off. Within experimental error, the points plotted in Figure 17 are distinct. That the rates are so similar at three very different long-range distances suggests that the distances evaluated from the native crystal structure are incorrect.

A recently performed crystal structure of the pentaammineruthenium(histidine-48)ferrimyoglobin[77] supports this hypothesis, because the ruthenium-labelled histidine (His-48) is greatly extended from the protein surface in the crystalline state. The iron to ruthenium distance observed in the crystal structure is ~24 Å, in contrast to the calculated metal to metal separation of ~18 Å in the modified native structure. The fact that the histidine residue can reorient itself by

Table 6. Intersite and closest ligand distances evaluated from the modified native myoglobin crystal structure.

a_5Ru(His)Mb	metal-metal (Å)	edge-edge (Å)	k_f (s^{-1})	$\ln(k_f)$
His-12	28.8	22.1	101± 11	4.62± 0.11
His-48	17.7	13.3	70± 8x10^3	11.16± 0.10
His-81	23.2	19.2	86± 12	4.45± 0.26
His-116	27.4	20.4	89± 3	4.49± 0.03

Figure 17. Plot of $\ln(k_f)$ versus distance for a_5Ru(His)Mb(^{3}ZnP*). Distances were determined from the native protein crystal structure. Metal-to-metal separations are designated by triangles and edge-to-edge distances by diamonds.

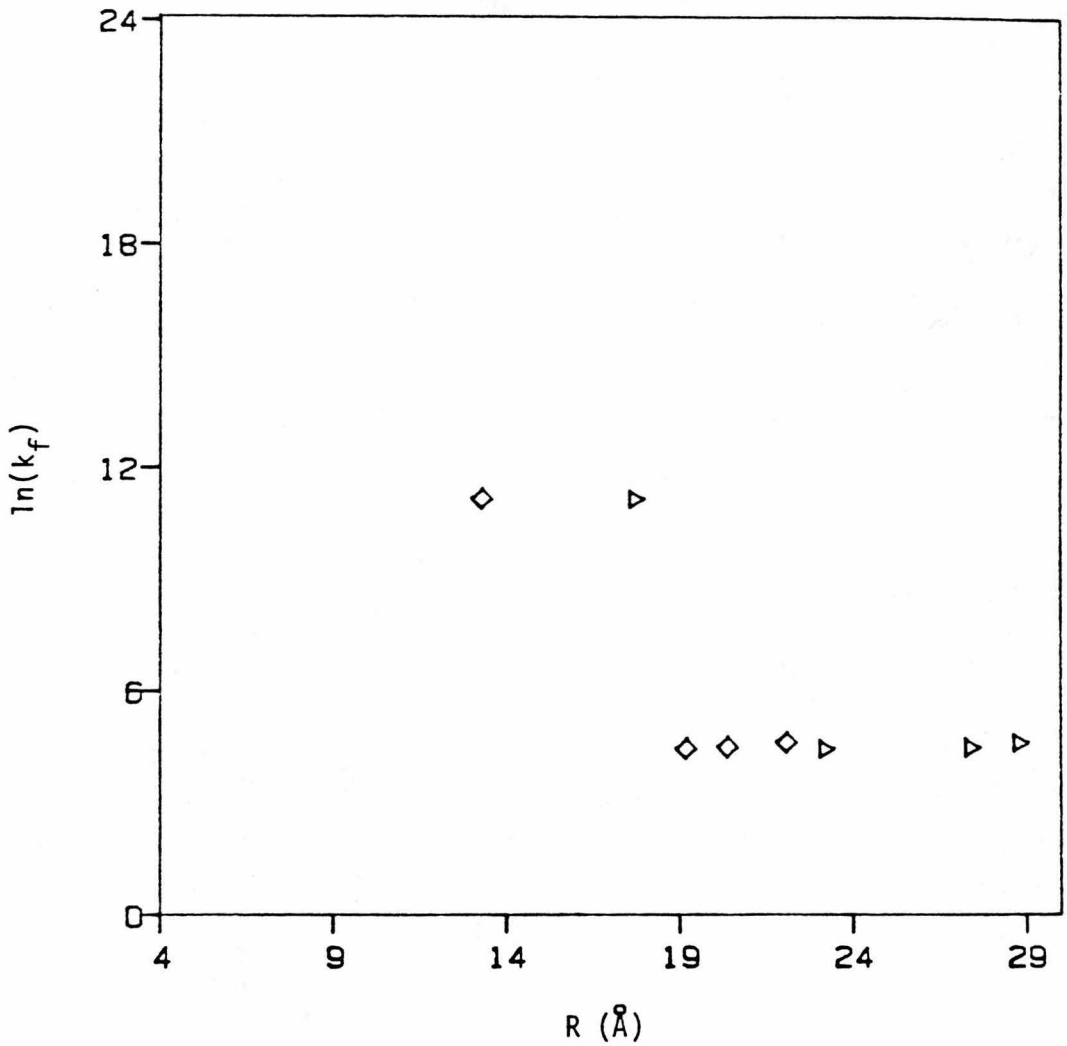
24
18
12
6
0
ln(k_f)
4
9
14
19
24
29
R (Å)

rotating about the C_α - C_β bond indicates that the through-space separations should be reevaluated to optimize the distances.

Computer-graphics imaging studies were used to reassess the intramolecular through-space distances. The metal-to-metal minimum distances are quite similar to the values estimated from the native structure (Table 7). Better agreement, however, is seen in the edge-to-edge data where the distances of the His-81 and His-116 are now nearly identical (Figure 18).

The rate of a fixed-site intramolecular reaction is given by Equation 4,

$$k = \kappa\nu \exp(-\Delta G^*/RT). \quad (4)$$

In the nonadiabatic case ($\kappa << 1$), when the donor and acceptor are weakly coupled, $\kappa\nu$ may be approximated as,[72]

$$\kappa\nu \propto H_{AB}^2. \quad (5)$$

The electronic coupling matrix element, H_{AB}, decreases exponentially with distance in many cases (Equation 3), so

$$\kappa\nu = 1x10^{13} \exp(-\beta(R - R_o)) \ s^{-1} \quad (6)$$

where $\beta = 2\alpha$ and $1x10^{13}$ s^{-1} is the assumed nuclear frequency at van der Waals contact, $R = R_o$. Under such conditions, the adiabaticity of the reaction approaches unity. The electron-transfer rate between

Table 7. Distance ranges evaluated from nonbonded repulsions at the protein surface.

a_5Ru(His)Mb	metal-metal (Å)	edge-edge (Å)	k_f (s^{-1})	$\ln(k_f)$
His-12	28.8-30.4	22.1-22.4	101± 11	4.62± 0.11
His-48	18.6-24.1	13.4-16.6	70± 8x10^3	11.16± 0.10
His-81	26.3-26.9	19.0-19.4	86± 12	4.45± 0.26
His-116	23.1-27.8	18.9-20.4	89± 3	4.49± 0.03

Figure 18. Plot of $\ln(k_f)$ versus distance for a_5Ru(His)Mb(^{3}ZnP*). Distances were determined from optimized rotations of the C_α - C_β bond in the labelled residues. Metal-to-metal separations are designated by triangles and edge-to-edge distances by diamonds.

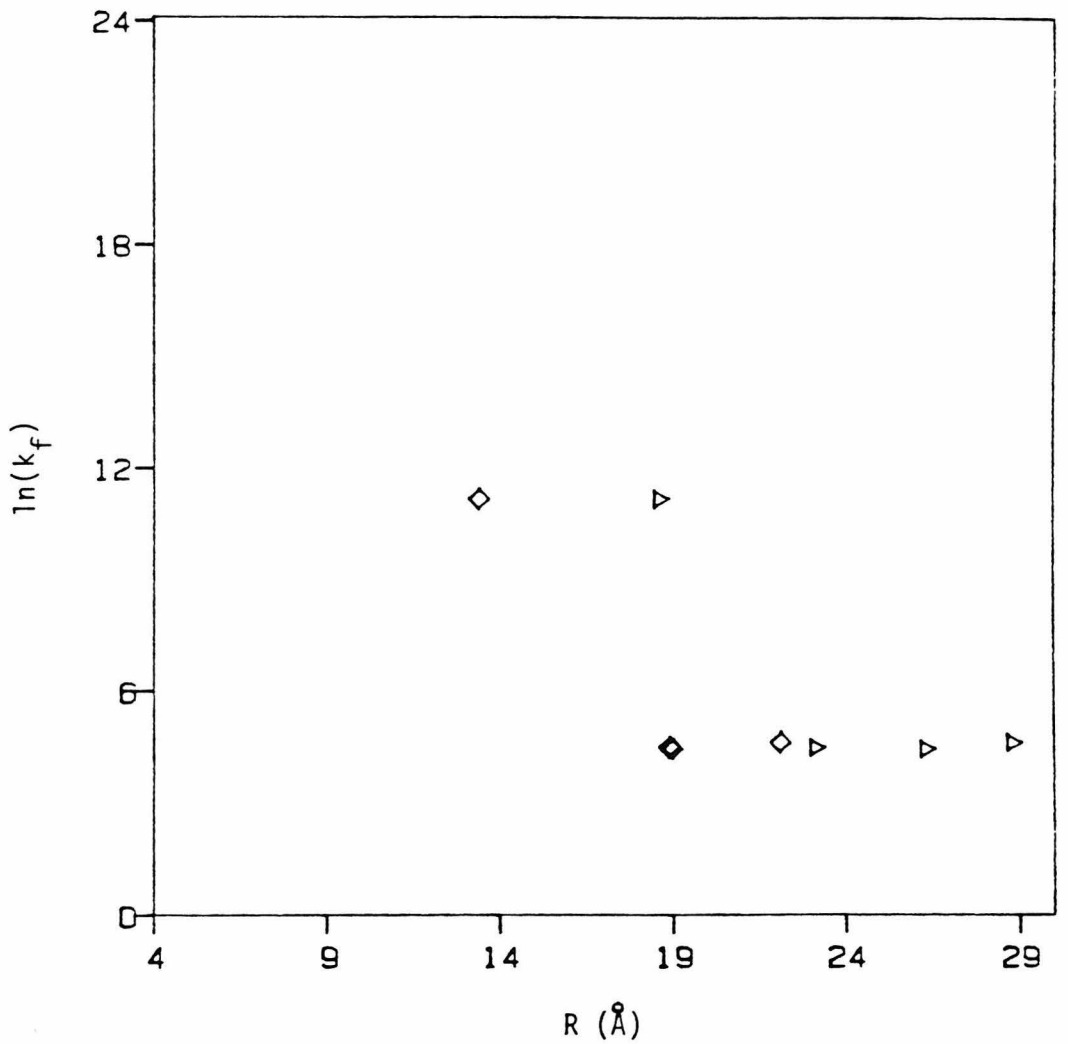
24
18
12
6
0
ln(k_f)
4
9
14
19
24
29
R (Å)

fixed sites may then be expressed as

$$k = 1x10^{13} \exp(-\Delta G^{*}/RT) \exp(-\beta(R - R_o)) \ s^{-1} \quad (7)$$

or more simply,

$$k = k_o \exp(-\beta(R - R_o)). \quad (8)$$

Fitting the rate-distance data from the His-48, 81, and 116 systems to Equation 10 with R_o = 4 Å (van der Waals contact at the porphyrin edge), $k_o(4\ Å) = 6x10^9\ s^{-1}$ and β = 1.2 $Å^{-1}$ (Figure 19). The intercept, $k_o(4\ Å)$, is several orders of magnitude lower than predicted. Since two different activation enthalpies have been measured in the zinc/ruthenium myoglobins, no direct allowance for an activated process can be made in order to adjust the distance term's prefactor. As protein conformational changes are believed to be reflected in the activation enthalpies, any structural perturbations may alter the calculated distances. A link between distance and activation enthalpy through protein conformational changes may require a more intricate treatment in order to adjust the value of $k_o(4\ Å)$. Nonetheless, β compares favorably with the theoretical estimate of 1.4 $Å^{-1}$ for carbon atoms in a π-bonding configuration[7,8] and experimental results of 1.2 $Å^{-1}$ from electron-transfer reactions between aromatic molecules in rigid matrices.[8]

Given the rate expression in Equation 8, rate-distance values for the His-12 modification can be calculated. For a rate of 100 s^{-1}, a

Figure 19. Analysis ($k = k_o \exp(-\beta(R - R_o))$) of $\ln(k_f)$ versus distance data. Rate-distance data for His-48, 116, and 81 are included.

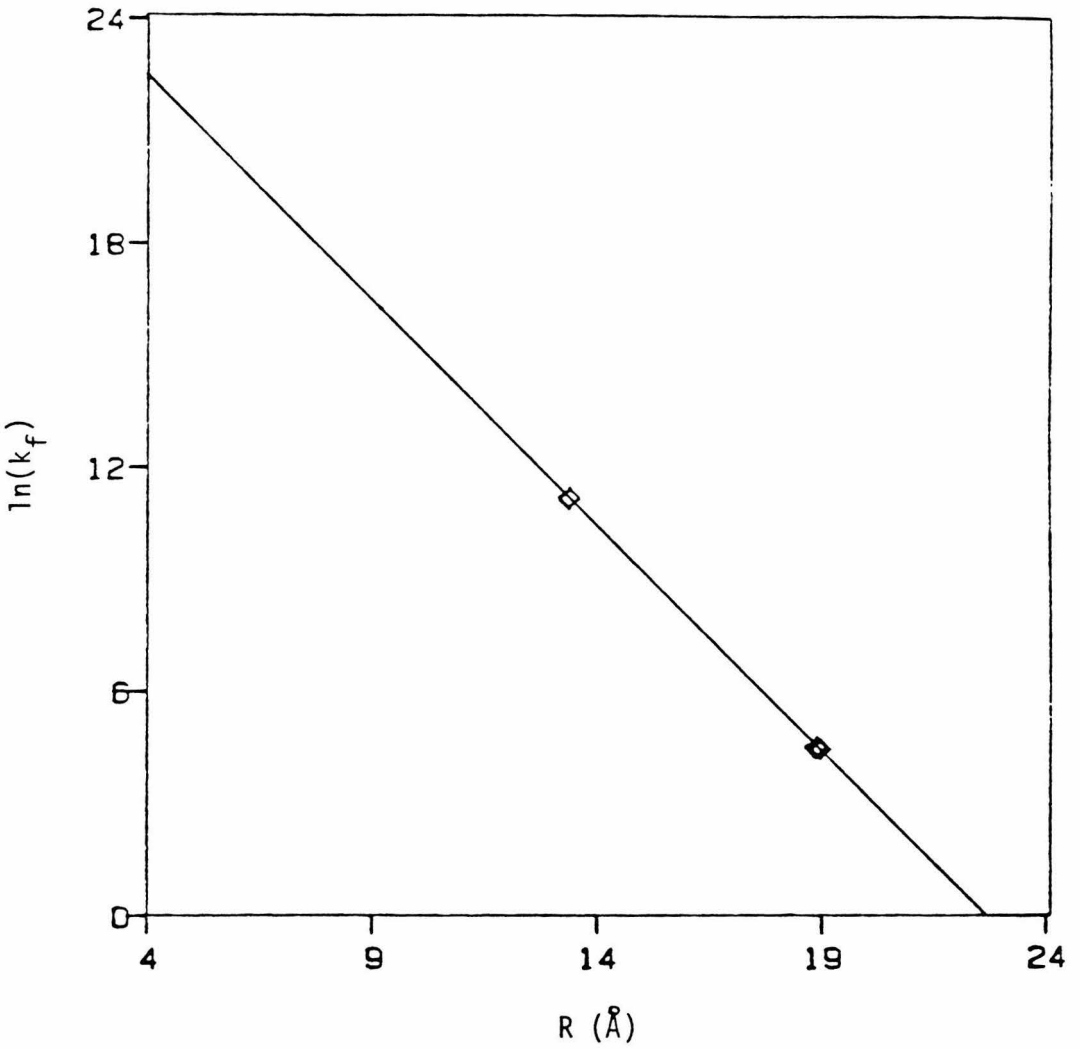
24
18
12
6
0
ln(k_f)
4
9
14
19
24
R (Å)

distance of 18.8 Å is obtained. Alternatively, a distance of 22.1 Å yields a rate of 2.0 s^{-1}. Two factors that could possibly account for this anomaly are the donor-acceptor orientation and the nature of the intervening protein medium.

Orientation Angles:

The orientation angle was measured between the line of the optimized through-space intersite pathway and the plane of the porphyrin. The orientation angles, 20° (His-12), 25° (His-48), 25° (His-81), and 35° (His-116) are quite similar for all four sites. This suggests that the anomalously fast rate of electron transfer in the His-12 derivative is not a result of an orientation effect.

Medium Effects:

Using computer-graphics methods, the protein residues that lie in the through-space pathways were determined (Figure 20). The His-48 medium has no protein residues that appear within van der Waals interaction limits of the reaction pathway. This medium, without any intervening components, can be taken as a convenient "neutral" reference. Aliphatic residues, isoleucine-75 and isoleucine-112, are not expected to influence the electronic coupling in the His-81 and His-116 pathways. The aromatic side chain of histidine-82 lies near the pathway to His-81. The plane of the His-82 ring is perpendicular to the through-space pathway. This unfavorable orientation (at a distance of 8 Å from His-81) is not expected to increase the electronic coupling.[72] The nearly identical rate-distance data for the His-81

Figure 20. Intervening residues on through-space pathways between ruthenium-labelling sites and porphyrin in myoglobin.

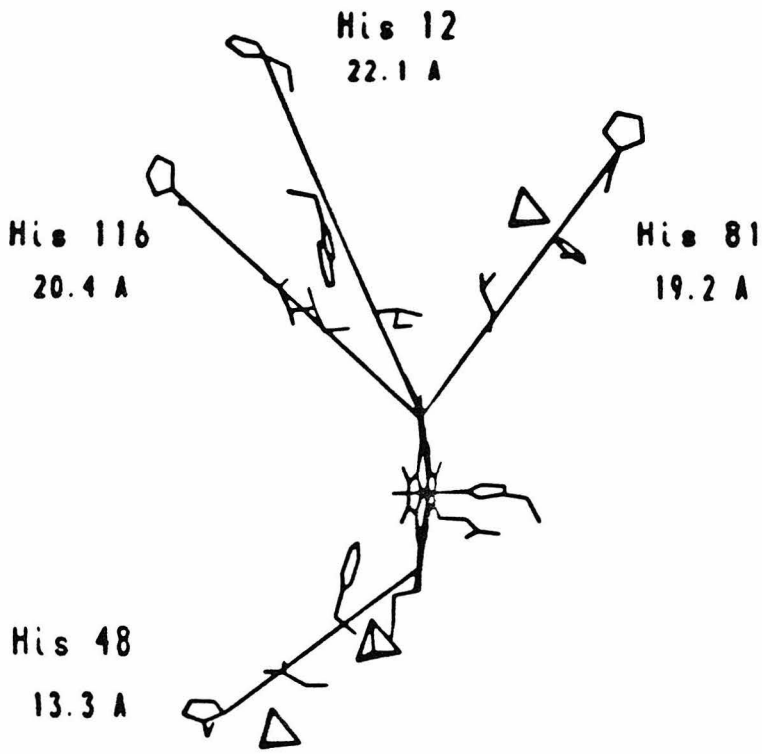
His 12
22.1 A
His 116
20.4 A
His 81
19.2 A
His 48
13.3 A

and His-116 derivatives can now be understood in terms of the similarintervening media in their through-space electron-transfer pathways. As no residues are expected to influence the electronic coupling in the pathways of His-48, 81, and 116, these three derivatives are considered "medium neutral" with respect to each other.

The His-12 medium contains a tryptophan residue (Trp-14). Unlike His-82, Trp-14 contains an aromatic ring that is oriented parallel-planar to the porphyrin, thereby providing evidence that the His-12 pathway is unique among those in the derivatized myoglobin systems. Theoretical calculations assuming a nearly optimal orientation indicate that the Trp-14 may enhance the electronic coupling by the equivalent of 3 Å.[79] Subtraction of this amount from the measured edge-to-edge distance reduces the "effective" distance of the His-12 pathway to 19 Å. This is in excellent agreement with the predicted distance (18.8 Å) based on the observed rate.

In accordance with earlier work,[80] the effect of medium can be substantial in influencing intramolecular electron-transfer kinetics. The rate-distance relationship derived from the myoglobin data provides a direct determination of the "effective" pathway length.

CHAPTER IV

Implications

In this section, the implications of the distance dependence of long-range electron transfer in the zinc/ruthenium-modified myoglobins are discussed with respect to other recent studies. First, recent kinetic data for the very similar zinc/ruthenium-modified cytochrome *c* as well as other metalloprotein systems are compared with the results from this work. Second, the through-space rate-distance relationship extracted from the zinc/ruthenium myoglobin experiments is discussed in light of results from organic model systems where electron transfer is proposed to proceed by a through-bond mechanism. Next, the kinetically rapid long-range electron-transfer rates observed in photosynthetic reaction centers are considered in the context of the zinc/ruthenium myoglobin edge to edge separation distances. Finally, directions for continuing and future investigations in the field of long-range intraprotein electron transfer are discussed.

Another a_5Ru(His)protein(ZnP) System:

The kinetic results for the zinc/ruthenium-modified cytochrome *c* may be utilized to extend the range of distances employed to fit Equation 8. This system is ideal to compare with the zinc/ruthenium-modified myoglobins, because the same donor and acceptor are present. The only major change is the intersite distance, as the driving force is essentially the same. In a_5Ru(His-33)Cyt *c*(ZnP), the edge-to-edge distance is 11.7 Å, as determined by computer modelling, and the intervening medium contains nonaromatic residues.[81] The observed electron-transfer rate in this system, 7.0×10^5 s^{-1}, compares closely with that predicted from Equation 8 (5×10^5 s^{-1}).[66] Inclusion of the

a_5Ru(His-33)Cyt *c*(ZnP) value yields a refined fit of the $\ln(k_f)$ versus distance plot,

$$k = 8x10^9 \exp(-1.2Å^{-1}(R - 4))\ s^{-1} \qquad (9)$$

where, as before, $R - 4 \geq 0$ (R in Å) (Figure 21). This expression will be used in the discussion that follows.

[Zn, Fe] Hybrid Protein-Protein Complexes:

The highly reducing nature of $^3ZnP^*$ has been utilized by other research groups to study intramolecular electron transfer in both multisite metalloproteins and protein-protein complexes. The metal centers in these systems are hemes. The general strategy has been to replace one (or two) of the hemes with zinc porphyrin. Electron transfer is then studied from $^3ZnP^*$ to the Fe^{3+}-heme.

One well-characterized system of this type is zinc/iron hybrid hemoglobin ([Zn, Fe]Hb).[21] In this system, zinc porphyrin is substituted into two of the hemoglobin subunits, producing the mixed metal [α_1^{Fe}, β_1^{Zn}, α_2^{Fe}, β_2^{Zn}] hybrid. Crystallographic data for native hemoglobin have been used to determine the distances and orientations of the various porphyrin pairs. The α_1^{Fe}-β_1^{Zn} site-to-site distance is very long (35 Å) compared with the shorter α_1^{Fe}-β_2^{Zn} distance of ~ 25 Å. The edge to edge distance between the porphyrin rings is about 20 Å. The porphyrins in the α_1^{Fe}-β_2^{Zn} pair are favorably oriented, that is, they are nearly parallel-planar.

The electron-transfer rate ([$^3ZnP^*$, Fe^{3+}]Hb → [ZnP^+, Fe^{2+}]Hb),

Figure 21. Plot of $\ln(k_f)$ versus distance for four $a_5Ru(His)$-protein(ZnP) experiments.

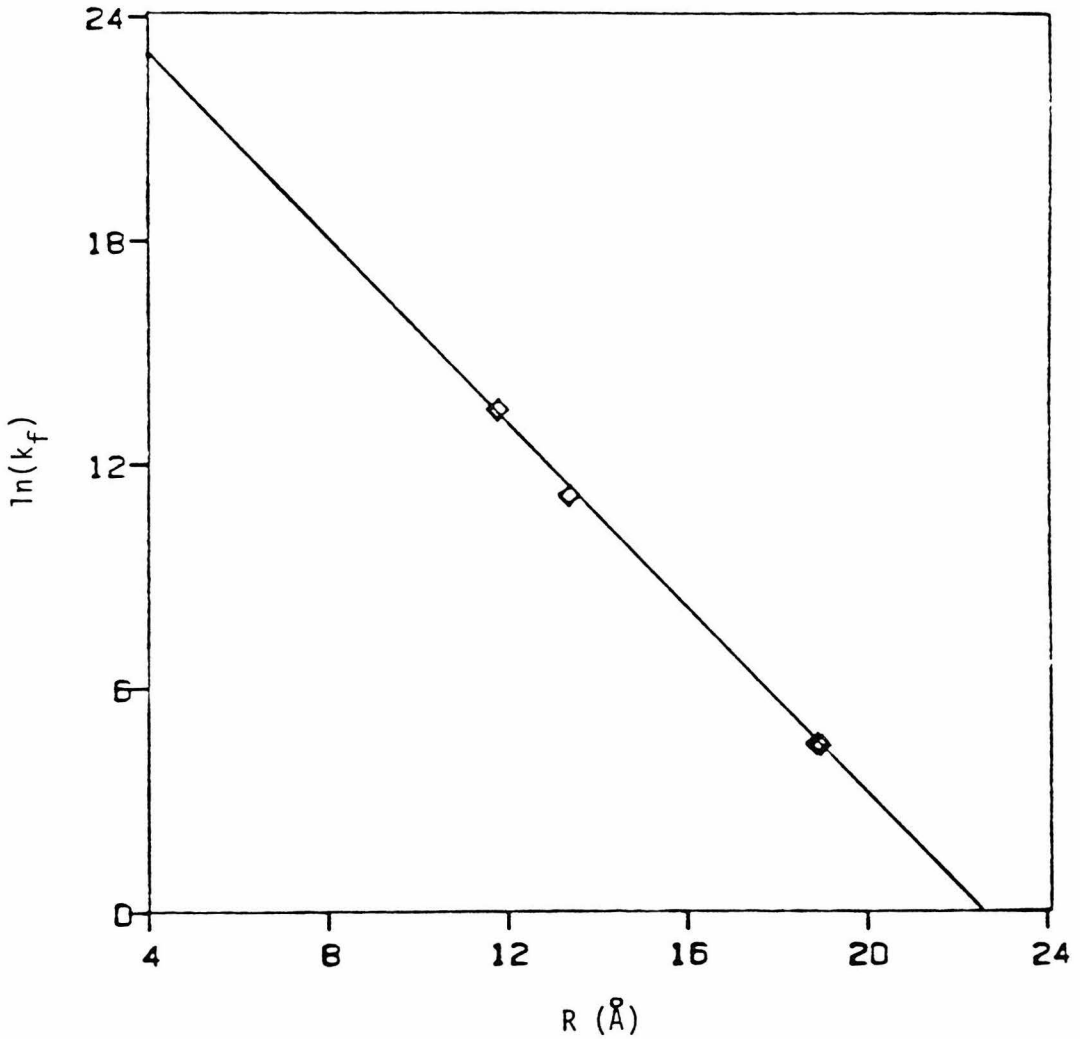
24
18
12
6
0
ln(k_f)
4
8
12
16
20
24
R (Å)

determined by transient absorption spectroscopy, is 100 ± 10 s^{-1}.[82] From the revised rate-distance expression (Equation 9), the rate at 20 Å is predicted to be 24 s^{-1}, a value that is considerably smaller than observed experimentally. This discrepancy, though not very great, is similar to that encountered in the a_5Ru(His-12)Mb(ZnP) rate-distance comparisons.

A possible explanation for this minor discrepancy is that the crystal structure represents an expanded conformation of the hemoglobin subunit chains, perhaps because of waters of hydration that are rigidly incorporated into the crystalline protein structure. In solution, however, relaxation of the crystalline rigidity requirements enables the waters to move freely and thereby allows the protein to recover from its expanded structure, resulting in a reduction of the intersite distance. This relaxation is expected in myoglobin as well. Though specific protein regions may exhibit greater flexibility than others, the molecular-scale compression and extension of the protein appear to be largely isotropic.[70] The rate-distance relationship in the zinc/ruthenium-modified myoglobins should be valid, because the same protein structure is involved in every experiment.

Such a difference between the crystal structure and solution conformation should be detectable as a discontinuity in the electron-transfer rates as the solution is frozen into a glass. At the lowest solution temperature, the compressed conformation would have a faster rate than the highest glass temperature. Electron-transfer rates in the solution (250 - 310 K) and solid (77 - 175 K) phase regions have been observed in [Zn, Fe]Hb, but in the critical temperature range,

near the freezing point of the glass, no data have been reported.[82] A close examination of the temperature effects in both [Zn, Fe]Hb and Zn/Ru-Mb is needed.

More recent work has involved protein-protein complexes. These systems utilize crystallographically characterized single-site metalloproteins that form stable and specific complexes. The distance of the electron-transfer reaction is evaluated by using computer-generated models of the docked protein-protein complex.

The complex formed between cytochrome b_5 and the zinc-substituted derivative of hemoglobin ($[\alpha_2^{Zn}, \beta_2^{Fe(III)CN}]$Hb) has been studied.[22] The edge-to-edge distance between the coplanar porphyrins, 7 - 8 Å (16 Å metal-to-metal), was evaluated by computer graphics simulation of the complex.[83] A rate of 8×10^3 s^{-1} has been reported for the $^3ZnP^*$-Fe^{3+} → ZnP^+-Fe^{2+} electron-transfer reaction, where the driving force is comparable to that reported in the hybrid hemoglobin system.

In the complex between zinc-substituted cytochrome *c* and cytochrome b_5, the model structure predicts an 8 Å edge-to-edge separation (17 Å metal to metal) between the porphyrin rings.[84] The driving force is similar to the other Zn/Fe-hybrid systems ($\Delta E^\circ \sim 0.85$ V), and the observed rate is 5×10^5 s^{-1}.[23]

One final Zn/Fe system that has been investigated consists of the physiologically relevant complex between yeast cytochrome *c* peroxidase and cytochrome *c*. Zinc has been substituted into the cytochrome *c* peroxidase. From modelling studies with the data from individual single-crystal X-ray diffraction structures, the porphyrin rings were found to be nearly parallel with an edge-to-edge distance of 17 - 18

Å.[85] The electron-transfer rate is 138 ± 12 s^{-1} at a driving force of ~ 0.90 V.[24]

The results from these protein-protein complex studies are summarized in Table 8. These rate-distance data are graphically compared with the distance-dependence results (Equation 9) in Figure 21. In general, the distances associated with the observed rates in the protein-protein complexes are too short with respect to the zinc/ruthenium-modified myoglobin results. A possible explanation for the low distance estimates is that the protein-protein complexes do not pack as well at the interface as assumed in the computer modelling. The intervening medium could also bear on the issue, although a mechanism for electronic decoupling rather than enhancement is needed. A possible distinguishing feature of the protein-protein complexes is that electron transfer may occur across an aqueous interface between the two proteins. The donor-acceptor electronic coupling could be adversely affected by such an intervening polar environment.

Currently, experiments involving protein-protein complexes are investigating medium effects.[80] In these studies, a phylogenetically conserved phenylalanine (Phe-87) in yeast cytochrome *c* (C*c*) is believed to mediate electron transfer between cytochrome *c* and cytochrome *c* peroxidase (C*c*P). Through site-directed mutagenesis, the phenylalanine is replaced with tyrosine (Tyr), serine (Ser), and glycine (Gly). The Phe and Tyr contain aromatic side chains (tolyl and *p*-hydroxytolyl, respectively), serine contains a heteroatom (hydroxymethyl), and glycine contains a hydrogen. The long-range electron-transfer kinetics are studied within the protein-protein

Table 8. Observed and calculated rate data for Zn/Fe-hybrid protein-protein complexes.

Protein-Protein Complex	k_{obs} (s^{-1})	$\ln(k_{obs})$	R (Å)	k_{calc}[a] (s^{-1})
$[^3ZnP^*, Fe^{3+}]$Hb/Cyt b_5 (Fe^{3+})	$8x10^3$	8.99	7	$2x10^8$
($^3ZnP^*$)Cyt *c*/Cyt b_5 (Fe^{3+})	$5x10^5$	13.12	8	$6x10^7$
($^3ZnP^*$)C*c*P/Cyt *c* (Fe^{3+})	$1.4x10^2$	4.93	17	$9x10^2$

a. Calculated from Equation 9 with R values taken from computer-model studies (refs. 79-81).

complex between the zinc-substituted *Cc*P and the various *Cc* mutants.

The results of these studies show that the $Cc\text{P}(^3\text{ZnP}^*) \rightarrow Cc(\text{Fe}^{3+}\text{P})$ electron transfer proceeds at similar rates in the Phe, Tyr, and Ser containing cytochromes *c*. The Gly mutant exhibits a rate considerably slower. More significantly, the reverse reaction, $Cc(\text{Fe}(^{2+}\text{P}) \rightarrow Cc\text{P}(\text{ZnP}^+)$, is four orders of magnitude faster in the Phe and Tyr modifications than in the Ser and Gly. The absence of a medium effect in the $Cc\text{P}(^3\text{ZnP}^*) \rightarrow Cc(\text{Fe}^{3+}\text{P})$ electron transfer may easily be attributed to an improper orientation of the intervening aromatic residue. Conformational changes are associated with the reduction of the ferricytochrome *c*. These changes may bring the aromatic residues into a favorable orientation for the very rapid $Cc(\text{Fe}(^{2+}\text{P}) \rightarrow Cc\text{P}(\text{ZnP}^+)$ reverse reaction. Alternatively, the conformational changes may diminish the intersite distance. Though the detailed explanation of these electron-transfer rates is not known, the observation that the direction of electron transfer can have a profound effect on the rate suggests further lines of research.

Rigid Organic Linkers:

In addition to biologically relevant systems discussed above, synthetic models that incorporate aromatic donors and acceptors linked by rigid organic spacers have been employed in the investigation of intramolecular electron transfer. In one system, the electron donor is a biphenyl radical anion generated from a bimolecular reaction with solvated electrons. The spacer is a rigid, steroidal skeleton. The acceptor is one of a series of organic molecules with a π-electron

network (for example, naphthyl and quinonyl) (Figure 22a). The electron-transfer rate was measured by time-resolved monitoring of the radical anion transient absorption.[86,87] With a driving-force range from 0 to 2.4 V, the observed rates are 10^6 to 10^9 s^{-1} at an edge to edge distance of 10 Å. The maximum rate was found at a driving force of ~1.2 V.

In a similar system, the spacer, a rigid, aliphatic bridge, separates the electron donor, a photoexcitable naphthalene chromophore, from a cyanoethylene acceptor (Figure 22b).[88] Spacers were added or removed to vary the range from 7 to 15 Å. Rates at distances of 9 Å are greater than 10^{11} s^{-1}. An increase in the spacer length (to ~14 Å) results in an electron-transfer rate at least two orders of magnitude slower.

A third system incorporates an aromatic phenyl (or biphenyl) bridge to separate a dimethylaniline donor from a photoexcited anthracene acceptor (Figure 22c).[89] Electron-transfer rates as fast as 10^9 s^{-1} were observed at a distance of 7.5 Å. Increasing the distance by 4 Å with another phenyl spacer caused the rate to fall by only 20 - 30 times.

A final system utilizes a photoexcited metalloporphyrin donor attached to a quinone acceptor by a bicyclo[2.2.2]octane spacer (Figure 22d).[90] At a distance of 10 Å, electron transfer takes place at 10^9 s^{-1} (ΔE° ~ 1.0 V). With the addition of another spacer, the rate falls by two orders of magnitude.

From Equation 09, the predicted electron-transfer rate is 5×10^6 s^{-1} at a distance of 10 Å. This value is similar to the low-driving

Figure 22. Structures of donor-spacer-acceptor systems, a) biphenyl-steriod-naphthyl (R = 10 Å), b) naphthalene-bridge-cyanoethylene (R = 9 Å), c) dimethylaniline-phenyl-anthracene (R = 7.5 Å), and d) porphyrin-linker-quinone (R = 10 Å). Edge-to-edge donor-acceptor distances are indicated.

a)

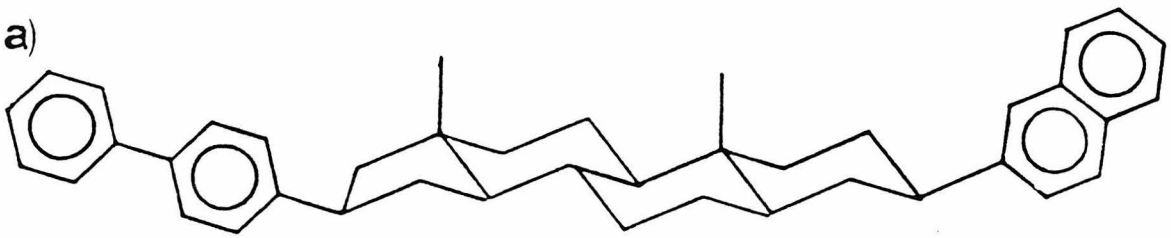

b)

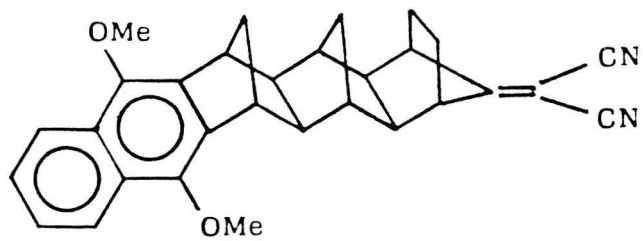

c)

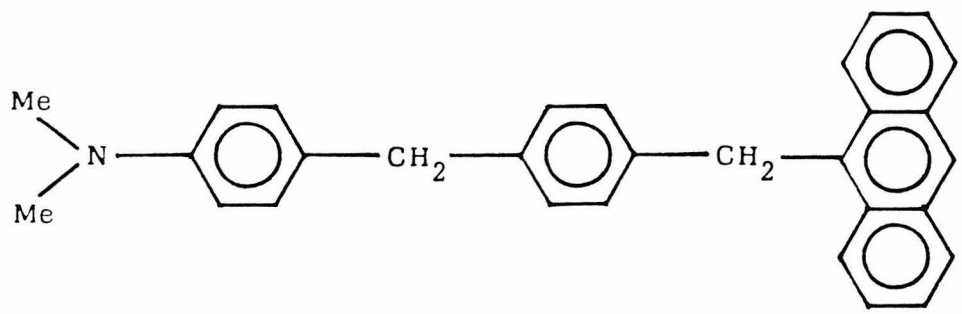

d)

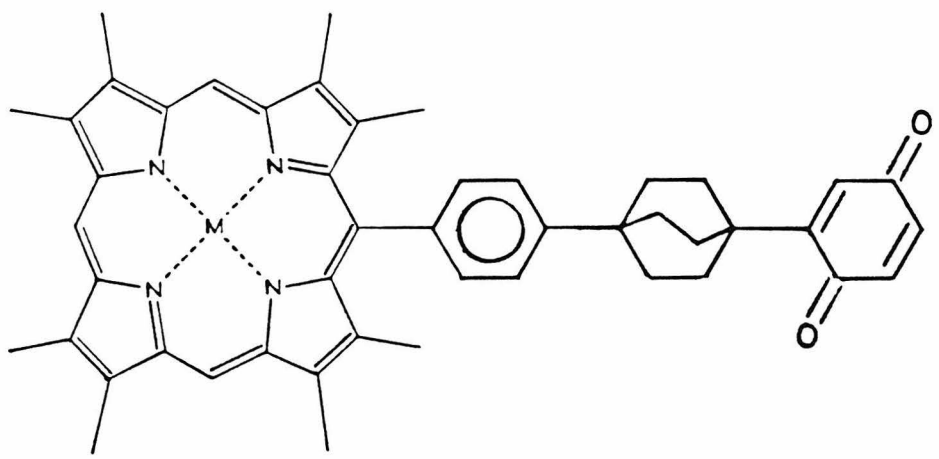

force rate, 10^6 s^{-1}, reported in the biphenyl-steroid-naphthyl system. Furthermore, the rate dependence on distance through a saturated linker falls off in a fashion similar to the intraprotein rate-distance dependence determined in this work (~10^2 s^{-1} for ΔR = 4 Å). In the presence of an aromatic spacer, however, the rate falls less dramatically, suggesting that the π-interactions available to the aromatic system may enhance the electronic coupling.[91] The importance of the intervening medium, in particular an aromatic-group enhancement of the donor-acceptor coupling as proposed for the $^3ZnP^*$ → a_5Ru^{3+} electron transfer in a_5Ru(His-12)Mb(ZnP), is indicated by these experimental results. While the structures of these systems and the rapid rates they exhibit may suggest that the electron transfers take place by a through-bond mechanism, the similarity with the distance dependence in the through-space intraprotein work indicates that the through-bond and through-space long-range coupling effects are the same. The reason for the slower rates observed in the zinc/ruthenium myoglobins may be an artifact of the activated electron-transfer processes that occur in them.

Photosynthetic Reaction Center:

The electron-transfer kinetics of the primary charge-separation step will be considered here, as it is analogous to the reactions measured in the zinc/ruthenium-modified myoglobins. The spatial relationships of the prosthetic groups that constitute the photosynthetic reaction center in the bacterium *Rhodopseudomonas viridis* have recently been elucidated.[92] The groups involved in the initial elec-

tron-transfer events consist of a bacteriochlorophyll *b* dimer, $(BChl)_2$, two monomeric bacteriochlorophylls *b*, BChl, and two bacteriopheophytin *b* molecules, BPh. The components of the dimer lie in close proximity to each other with their pyrrole rings separated by as little as 3 Å. A BChl is associated with each BChl in the dimer. The porphyrin-ring separation appears to be about 3.5 Å. A BPh is then positioned about 4 Å (closest approach) to each of the monomeric BChl's.

The rate of formation of $BChl^-$ from $(BChl)_2^*$ has been reported to be 10^{12} s^{-1}.[72] The subsequent rate of reduction of BPh is $2x10^{11}$ s^{-1}.[72] The activation free energies of these reactions are negligibly small. For electron-transfer reactions across distances of 3.5 and 4 Å, the rates predicted by Equation 9 are $1x10^{10}$ s^{-1} and $8x10^9$ s^{-1}, respectively.

The arrangement of components in the photosynthetic reaction center does not favor a through-bond electron-transfer mechanism. Within the framework of a through-space mechanism, the rapid electron-transfer rates would need to be activationless, given the results from the fixed-site Zn/Ru-hybrids. The driving forces for these reactions are less than in the zinc/ruthenium-modified proteins, indicating that the reorganization energy must be correspondingly lower. The reaction center appears to be a finely tuned system that minimizes donor-acceptor distance and reorganization energy to allow extremely rapid electron transfers to take place.

Directions of Future Work:

This study on zinc/ruthenium-modified myoglobins has revealed a long-range intraprotein electron-transfer rate dependence on distance. Promising areas for continuing and future investigation include a) an extension of the range of electron-transfer distances for the zinc/ruthenium-modified proteins, b) determination of the low-temperature properties of intraprotein electron transfer, and c) measurement of the dependence of the rate on driving force in the ruthenium-modified metalloprotein systems.

The temperature dependence of the electron transfer rates in the a_5Ru(His)Mb(ZnP) system should be examined at low temperature in order to assess the importance of tunneling as well as the freezing of protein conformational motions. Preliminary work with optically detected magnetic resonance in the a_5Ru(His)Mb(ZnP) systems indicates that the electron-transfer rates in the four derivatives are about the same (2 s^{-1}) at 4 K. That the rates are slow at low temperature is not surprising, though a_5Ru(His-48)Mb(ZnP) was expected to show a measurably faster rate at 4 K in comparison with its longer-ranged counterparts. His-48 may exist in an extended conformation in which the edge-to-edge distance is nearly 17 Å, which is comparable to the other sites. If this is the conformation of the protein in a frozen glass, it would explain the similarity of the low-temperature rates. By approaching the melting temperature of the glass from above and below, information concerning the proposed conformational changes should be obtained.

One way to change the driving force is to vary the me-

talloporphyrin that is inserted into the ruthenium-modified myoglobin. Ideally, the metalloporphyrins selected should exhibit phophorescence in solution at room temperature and have triplet lifetimes of at least 1 ms. Triplet lifetimes less than 1 ms are too short to allow electron-transfer quenching at long distances. Preliminary work with palladium-mesoporphyrin IX (PdP) (Pd^{2+} as the central metal: Pt^{2+}, Rh^{3+}, and Sn^{4+} are other possibilities) demonstrates the feasibility of this line of attack.

Palladium-mesoporphyrin IX was inserted into ruthenium-labelled myoglobin derivatives in the same fashion as zinc porphyrin was. Mb(PdP) was successfully purified on a CM-52 column; however, a_5Ru(His-48)Mb(PdP) apparently denatured on the column.

Transient absorption (λ = 391 nm) and triplet emission (λ = 671 nm) measurements on Mb(PdP), performed on the pulsed laser system, yielded a triplet decay rate of 1.0×10^3 s^{-1} at 25°C. No triplet quenching was observed in a_5Ru(His-81)Mb(PdP). A biphasic triplet emission was seen in a_5Ru(His-48)Mb(PdP) with component rates of 8×10^3 s^{-1} and 1×10^1 s^{-1}. The complicated behavior in the emission by a_5Ru(His-48)Mb(^{3}PdP*) was attributed to impurities remaining from the incomplete purification procedure (no CM-52 column). The electron-transfer rate in a_5Ru(His-48)Mb(PdP) appears to be an order of magnitude slower than in the corresponding zinc system. Though ^{3}PdP* is of higher energy than ^{3}ZnP*, ~0.1 V, the cation radical is expected to be higher still, ~0.2 V. As a result, the driving force is expected to be ~0.1 V lower in the Pd/Ru-Mb than in the Zn/Ru-Mb, and may explain the slower electron-transfer rate observed. Slightly

longer lifetimes are needed in order to detect the electron-transfer reactions in the longer-ranged derivatives. The ability to monitor the phosphorescence of the triplet by time-resolved methods enhances the flexibility of conducting experiments with these electron-transfer systems.

In addition to studying driving force effects in the oxidative quenching by a_5Ru^{3+}, several metalloporphyrins (for example, $Sn^{4+}P$) should allow investigations of reductive quenching of the porphyrin excited state and in so doing enable observations of electron-transfer processes in the reverse direction. This could be particularly interesting, because recent theoretical work indicates that medium effects, especially those involving aromatic groups, should not be the same for oxidative and reductive quenching processes.[79]

APPENDIX A

Calculation of Model System Coordinates

The procedure employed to calculate the pentaammineruthenium coordinates using the Brookhaven crystallographic data base for sperm whale myoglobin is presented in this section. The details of the calculations for a_5Ru(His-48) derivative are shown. Pertinent coordinates and final results for the His-81, 116, and 12 derivatives are also included. The assumptions made about the position of the ruthenium relative to the imidazole ring are (Figure #):

1) Ruthenium is attached to the N_ε;
2) Ruthenium lies in the plane of the imidazole ring defined by C_δ - N_ε - C_ε;
3) The N_ε - Ru vector bisects the reflex angle, C_δ - N_ε - C_ε;
4) The coordination sphere of the ruthenium is octahedral.

The general procedure used to determine the ruthenium coordinates involves the definition of the C_δ - N_ε - C_ε plane and then solution of a set of linear equations in three variables. The linear equations are produced from the distance formula, $d^2 = x^2 + y^2 + z^2$, and the equation of the plane. The distances between the sought ruthenium coordinates, (x,y,z), and the C_δ and C_ε atoms of the imidazole ring are calculated based on a N_ε - Ru distance of 2.12 Å and criterion 2) mentioned above. Having determined the ruthenium coordinates, the direction vectors from the ruthenium to the vertices of an octahedron (the ammine ligand positions) are calculated. The Ru - NH_3 distance is taken as 2.12 Å.

$N_\varepsilon(x,y,z) = (30.874, 28.896, -1.164)$

$C_\varepsilon(x,y,z) = (29.747, 29.559, -1.315)$

$C_\delta(x,y,z) = (31.311, 28.457, -2.380)$

$Ru(x,y,z) = (x,y,z)$

	R^2	R
$\boldsymbol{N_\varepsilon C_\varepsilon} = -1.127\boldsymbol{i} + 0.663\boldsymbol{j} - 0.151\boldsymbol{k}$	1.732499	1.316244
$\boldsymbol{N_\varepsilon C_\delta} = 0.437\boldsymbol{i} + 0.439\boldsymbol{j} - 1.216\boldsymbol{k}$	1.862346	1.364678
$\boldsymbol{N_\varepsilon Ru} = (x - 30.874)\boldsymbol{i} + (y - 28.896)\boldsymbol{j} + (z + 1.216)\boldsymbol{k}$	4.494400	2.120000

Generate the normal vector of the ring plane, C_δ - N_ε - C_ε

$\boldsymbol{N_\varepsilon C_\varepsilon} \times \boldsymbol{N_\varepsilon C_\delta} = -0.872497\boldsymbol{i} - 1.436419\boldsymbol{j} + 0.205022\boldsymbol{k}$	2.866585	1.693099

Determine the angular position with respect to C_δ - N_ε - C_ε

$\|\boldsymbol{N_\varepsilon C_\varepsilon} \times \boldsymbol{N_\varepsilon C_\delta}\| / (\|\boldsymbol{N_\varepsilon C_\varepsilon}\| \, \|\boldsymbol{N_\varepsilon C_\delta}\|) = \sin \Phi = 0.942575$

$\Phi = 70.488542$ $\qquad \Phi' = 180 - \Phi = 109.511458$

$\Theta = 360 - \Phi' = 250.488542$ $\qquad \Theta/2 = 125.244271$ $\qquad \cos \Theta/2 = -0.577064$

Calculate the equation of the plane, requiring the Ru to be coplanar

$$\boldsymbol{N_\varepsilon Ru} \cdot \boldsymbol{N_\varepsilon C_\varepsilon} \times \boldsymbol{N_\varepsilon C_\delta} =$$

$$-0.872497x - 1.436419y + 0.205022z + 68.682881 = 0$$

$$-4.255626x - 7.006170y + z + 335.002492 = 0 \qquad \text{(A-1)}$$

Evaluate the distances to the Ru

$\|\boldsymbol{N_\varepsilon Ru}\|^2 = 4.494400$

Apply the Law of Cosines to determine the remaining two distances

$a^2 = b^2 + c^2 - 2bc \cos(\Theta/2)$

$\|C_\varepsilon Ru\|^2 = 9.447421$ where b = $\|N_\varepsilon Ru\|$ and c = $\|N_\varepsilon C_\varepsilon\|$

$\|C_\delta Ru\|^2 = 9.695774$ where b = $\|N_\varepsilon Ru\|$ and c = $\|N_\varepsilon C_\delta\|$

From the distance formula, generate three equations

$\|N_\varepsilon Ru\|^2 = (x - 30.874)^2 + (y - 28.896)^2 + (z + 1.164)^2 = 4.494400$

$x^2 + y^2 + z^2 - 61.748x - 57.792y + 2.328z + 1785.043188 = 0$ (A-2)

$\|C_\varepsilon Ru\|^2 = (x - 29.747)^2 + (y - 29.559)^2 + (z + 1.315)^2 = 9.447421$

$x^2 + y^2 + z^2 - 59.494x - 59.118y + 2.630z + 1750.900294 = 0$ (A-3)

$\|C_\delta Ru\|^2 = (x - 31.311)^2 + (y - 28.457)^2 + (z + 2.380)^2 = 9.695774$

$x^2 + y^2 + z^2 - 62.622x - 56.914y + 4.760z + 1786.148196 = 0$ (A-4)

Reduce quadratic equations to linear form

(A-4) - (A-2) = $-0.874x + 0.878y + 2.432z + 1.105008 = 0$

$-0.359375x + 0.361020y + z + 0.454362 = 0$ (A-5)

(A-3) - (A-2) = $2.254x - 1.326y + 0.302z - 34.142894 = 0$

$7.463576x - 4.390728y + z - 113.055940 = 0$ (A-6)

(A-4) - (A-3) = $-3.128x + 2.204y + 2.130z + 35.247902 = 0$

$-1.468545x + 1.034742y + z + 16.548311 = 0$ (A-7)

{(A-4) - (A-2)} - {(A-3) - (A-2)} = {(A-4) - (A-3)}, hence only two independent equations remain and an additional one is needed. The equation of the plane is used.

$-4.255626x - 7.006170y + z + 335.002492 = 0$ (A-1)

Now solve the system of three linear equations

(A-6) - (A-1) = 11.719202x + 2.615442y - 448.058432 = 0

$$4.480773x + y - 171.312701 = 0 \qquad \text{(A-8)}$$

(A-7) - (A-1) = 2.787081x + 8.040912y - 318.454181 = 0

$$0.346613x + y - 39.604237 = 0 \qquad \text{(A-9)}$$

(A-8) - (A-9) = 4.134160x - 131.708464 = 0

Final values are

x = 31.858579 y = 28.561639 z = 0.683455

Ru(x,y,z) = (31.859, 28.562, 0.683)

The vector $\boldsymbol{N_\varepsilon Ru}$ now provides the direction vector for $\boldsymbol{RuN_1}$

$\boldsymbol{N_\varepsilon Ru} = (x - 30.874)\boldsymbol{i} + (y - 28.896)\boldsymbol{j} + (z + 1.216)\boldsymbol{k}$

$\boldsymbol{N_\varepsilon Ru} = 0.985\boldsymbol{i} - 0.334\boldsymbol{j} + 1.847\boldsymbol{k} = \boldsymbol{RuN_1}$

Normal vector to the plane, C_δ - N_ε - C_ε.

$\boldsymbol{N} = -0.872497\boldsymbol{i} - 1.436419\boldsymbol{j} + 0.205022\boldsymbol{k}$

Convert normal vector to a normal vector with length 2.12, the Ru - NH_3 distance

$\alpha\boldsymbol{N} = -0.872497\alpha\boldsymbol{i} - 1.436419\alpha\boldsymbol{j} + 0.205022\alpha\boldsymbol{k}$

$\|\alpha\boldsymbol{N}\|^2 = (-0.872497\alpha)^2 + (1.436419\alpha)^2 + (0.205022\alpha)^2 = (2.12)^2$

$2.866585\alpha^2 = (2.12)^2$

$\alpha = 2.12/(2.866585)^{0.5} = 1.252142$

$N_{2.12} = -1.092490\boldsymbol{i} - 1.798600\boldsymbol{j} + 0.256717\boldsymbol{k} = \boldsymbol{RuN_2}$

$N_{-2.12} = 1.092490\boldsymbol{i} + 1.798600\boldsymbol{j} - 0.256717\boldsymbol{k} = \boldsymbol{RuN_4}$

Generate normal vector to plane containing N_1 - Ru - N_2

$\boldsymbol{RuN_1} = 0.985\boldsymbol{i} - 0.334\boldsymbol{j} + 1.847\boldsymbol{k}$

$\boldsymbol{RuN_2} = -1.092\boldsymbol{i} - 1.799\boldsymbol{j} + 0.257\boldsymbol{k}$

$\boldsymbol{RuN_1} \times \boldsymbol{RuN_2} = 3.236915\boldsymbol{i} - 2.270069\boldsymbol{j} - 2.136743\boldsymbol{k} = \boldsymbol{N_\perp}$

This vector provides the direction from Ru ot N_3 and N_5

Converting to vector length 2.12

$\alpha N_\perp = 3.236915\alpha\boldsymbol{i} - 2.270069\alpha\boldsymbol{j} - 2.136743\alpha\boldsymbol{k}$

$\|\alpha N_\perp\|^2 = (3.236915\alpha)^2 + (2.270069\alpha)^2 + (2.136743\alpha)^2 = (2.12)^2$

$20.196503\alpha^2 = (2.12)^2$

$\alpha = 2.12/(20.196503)^{0.5} = 0.471735$

$N_{\perp 2.12} = 1.526965\boldsymbol{i} - 1.070870\boldsymbol{j} - 1.007976\boldsymbol{k} = \boldsymbol{RuN_3}$

$N_{\perp -2.12} = -1.526965\boldsymbol{i} + 1.070870\boldsymbol{j} + 1.007976\boldsymbol{k} = \boldsymbol{RuN_5}$

Using the direction vectors generated with length 2.12, the coordinates of the five ammines follow from vector addition. Some distances are provided to confirm the octahedral structure of the ligand shell. The distance between *cis*-ammines should be 2.9981.

His-48

$N_{\varepsilon}(x,y,z)$ = (30.874, 28.896,-1.164)

$C_{\varepsilon}(x,y,z)$ = (29.747, 29.559, -1.315)

$C_{\delta}(x,y,z)$ = (31.311, 28.457, -2.380)

	$\|\|RuN\|\|$	$\|\|N_{\varepsilon}N\|\|$	$\|\|N_iN_{i+1}\|\|$
Ru(x,y,z) = (31.859, 28.562, 0.683)			
$N_1(x,y,z)$ = (32.844, 28.228, 2.530)	2.120	4.240	2.999
$N_2(x,y,z)$ = (30.766, 26.763, 0.940)	2.120	2.998	2.999
$N_3(x,y,z)$ = (33.386, 27.491, -0.325)	2.120	2.998	2.998
$N_4(x,y,z)$ = (32.951, 30.360, 0.427)	2.120	2.998	2.998
$N_5(x,y,z)$ = (30.332, 29.633, 1.691)	2.120	2.998	

His-81

$N_{\varepsilon}(x,y,z)$ = (-3.404, 23.826, 20.964)

$C_{\varepsilon}(x,y,z)$ = (-2.473, 22.904, 21.094)

$C_{\delta}(x,y,z)$ = (-2.853, 24.970, 20.469)

	$\|\|RuN\|\|$	$\|\|N_{\varepsilon}N\|\|$	$\|\|N_iN_{i+1}\|\|$
Ru(x,y,z) = (-5.451, 23.570, 21.451)			
$N_1(x,y,z)$ = (-7.498, 23.314, 21.938)	2.120	4.240	2.998
$N_2(x,y,z)$ = (-5.065, 24.238, 23.426)	2.120	2.998	2.998
$N_3(x,y,z)$ = (-5.843, 25.565, 20.853)	2.120	2.998	2.998
$N_4(x,y,z)$ = (-5.837, 22.901, 19.477)	2.120	2.998	2.998
$N_5(x,y,z)$ = (-5.059, 21.574, 22.050)	2.120	2.998	

His-116

$N_{\varepsilon}(x,y,z)$ = (18.265, 3.269, 10.484)

$C_{\varepsilon}(x,y,z)$ = (17.492, 3.255, 11.543)

$C_{\delta}(x,y,z)$ = (18.462, 4.552, 10.080)

	$\|\|RuN\|\|$	$\|\|N_{\varepsilon}N\|\|$	$\|\|N_iN_{i+1}\|\|$
Ru(x,y,z) = (19.083, 1.553, 9.545)			
$N_1(x,y,z)$ = (19.901, -0.163, 8.606)	2.120	4.240	2.999
$N_2(x,y,z)$ = (17.374, 1.422, 8.297)	2.120	2.998	2.999
$N_3(x,y,z)$ = (20.036, 2.791, 8.112)	2.120	2.998	2.998
$N_4(x,y,z)$ = (20.791, 1.684, 10.794)	2.120	2.998	2.998
$N_5(x,y,z)$ = (18.130, 0.315, 10.978)	2.120	2.998	

His-12

$N_{\varepsilon}(x,y,z)$ = (14.402, 9.233, 24.945)

$C_{\varepsilon}(x,y,z)$ = (14.120, 9.934, 26.019)

$C_{\delta}(x,y,z)$ = (13.704, 9.719, 23.886)

	$\|\|RuN\|\|$	$\|\|N_{\varepsilon}N\|\|$	$\|\|N_iN_{i+1}\|\|$
Ru(x,y,z) = (15.743, 7.592, 24.875)			
$N_1(x,y,z)$ = (17.084, 5.951, 24.805)	2.120	4.240	2.999
$N_2(x,y,z)$ = (14.147, 6.269, 25.319)	2.120	2.998	2.998
$N_3(x,y,z)$ = (15.355, 7.364, 22.803)	2.120	2.998	2.998
$N_4(x,y,z)$ = (17.338, 8.915, 24.430)	2.120	2.998	2.997
$N_5(x,y,z)$ = (16.131, 7.821, 26.946)	2.120	2.998	

APPENDIX B

Kinetic Analysis

The derivation of the kinetic expression for the ground-state bleaching of the a_5Ru(His)Mb(ZnP) systems is presented. Given the proposed reaction mechanism

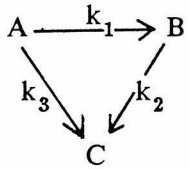

where k_1, k_2, and k_3 are the forward and reverse electron-transfer rate constant, and the intrinsic triplet-decay constant, respectively, A is the triplet excited state, $^3ZnP^*$-Ru^{3+}, B is the porphyrin cation radical, ZnP^+-Ru^{2+}, and C is the ground state, ZnP-Ru^{3+}. An expression for the time dependence of C following the excitation pulse is sought.

$$d[A]/dt = -k_1[A] - k_3[A] \qquad \text{(B-1)}$$

$$d[B]/dt = k_1[A] - k_2[B] \qquad \text{(B-2)}$$

$$d[C]/dt = k_3[A] + k_2[B] \qquad \text{(B-3)}$$

$$d[A]/[A] = -(k_1 + k_3)dt \qquad \text{(B-4)}$$

$$A = A_o \exp\{-(k_1 + k_3)t\} \qquad \text{(B-5)}$$

$$d[B]/dt + k_2[B] = k_1 A_o \exp\{-(k_1 + k_3)t\} \qquad \text{(B-6)}$$

multiplying both sides by $\exp\{k_2 t\}$

$$B = [k_1 A_o/(k_2 - k_1 - k_3)][\exp\{-(k_1 + k_3)t\} - \exp\{-k_2 t\}] \qquad \text{(B-7)}$$

$$d[C] = k_3 A_o \exp\{-(k_1 + k_3)t\} + [k_2 k_1 A_o/(k_2 - k_1 - k_3)] \quad \text{(B-8)}$$
$$[\exp\{-(k_1 + k_3)t\} - \exp\{-k_2 t\}]$$

$$C = A_o[1 + [(k_3 - k_2)/(k_2 - k_1 - k_3)]\exp\{-(k_1 + k_3)t\} + \quad \text{(B-9)}$$
$$[k_1/(k_2 - k_1 - k_3)]\exp\{-k_2 t\}]$$

From Equation B-9, the time dependence of the return to the ground state is a biphasic first-order exponential. In the event that $(k_1 + k_3)$ is much greater than k_2, or vice versa, the equation reduces to a single first-order expression. The forward electron-transfer rate constant, k_1, can be extracted from $(k_1 + k_3)$ by difference with the intrinsic decay rate, k_3.

APPENDIX C

Evaluation of Nonbonded Repulsions

The principal bond of rotation is C_α-C_β. This bond attaches the imidazole ring via a methylene (C_β) to the protein backbone. Rotation about this bond causes the maximum displacement of the side-chain residue. A secondary bond of rotation is C_γ-C_β. Rotation about this bond "flips" the imidazole ring. A 180° rotation essentially displaces the ruthenium pentaammine label to the C_ε.

Nonbonded repulsions between a_5Ru(His) and atoms at the protein surface were evaluated by van der Waals contact radii (Table C-1). Interaction distances for the various chemical substituents were determined by combining the appropriate covalent and van der Waals radii. These interaction radii were used to calculate the nonbonded repulsion distances in Table C-2.

Rotations were performed while monitoring interatomic distances at sites of potential repulsion. Upon reaching closest approach, an exhaustive search of interaction sites was made. The resulting metal-to-metal and edge-to-edge distances are presented in Table 7. The allowable ranges for the modified residues are included to indicate the local restrictions on each of the histidines.

The amount of extension allowed to each of the ruthenated histidines covered a considerable range, from only 0.6 Å in His-81 to 5.5 Å in His-48 (metal-to-metal). The maximum extension in His-48, 24.1 Å, compares well with the estimated distance in the a_5Ru(His-48)Mb crystal structure (~24 Å).[77] Bearing in mind that a protein is a dynamic molecule and that the crystal structure represents only one conformation, the histidines can be expected to rotate freely in aqueous solution.[93] The minimum accessible distances were selected as

Table C-1. Selected covalent and van der Waals radii of atoms.

	covalent radius[a] (Å)	v.d.Waals radius[b] (Å)
H	0.37	1.2
C	0.77	1.6
O	0.74	1.4
N	0.74	1.5
half-thickness of aromatic ring		1.7

Interaction radii of relevant groups are calculated from the appropriate covalent and van der Waals radii.

	(Å)
CH_3	2.0
OH $(O_{cov} + H_{cov}) + H_{vdW}$	2.3
NH_3 $(N_{cov} + H_{cov}) + H_{vdW}$	2.3

a. Wells, A. F. *Structural Inorganic Chemistry* Oxford University Press: New York **1962**.

b. Pauling, L. *The Nature of the Chemical Bond*, 3[d] ed., Cornell University Press: Ithaca, New York **1960**, p. 260.

Table C-2. Nonbonded repulsion distances calculated from covalent and van der Waals radii

Interaction Groups	Distance Å
CH_2 - OH	3.4
NH_3 - OH	3.7
CH_2 - CH_2	4.0
NH_3 - CH_2	4.3
NH_3 - NH_2	4.6

Other interaction distances are based on the initial crystallographic interatomic distances prior to any rotations or modifications.

amide - amide	3.2
amide - CH_2	3.6

the ranges for the rate-distance correlation (Figure 18). The metal-to-metal minimum distances are quite similar to the values estimated from the native structure (Table 6).

REFERENCES

and

NOTES

1. Hatefi, Y. *Annu. Rev. Biochem.* **1985**, *54*, 1015-1069.

2. Dixit, B. P. S. N.; Vanderkooi, J. M. *Curr. Top. Bioenerg.* **1984**, *13*, 159-202.

3. Michel-Beyerle, M. E., ed. *Antennas and Reaction Centers of Photosynthetic Bacteria* Springer-Verlag: Berlin **1985**.

4. Govindjee, ed. *Photosynthesis: Energy Conversion by Plants and Bacteria*, Vol. I, Academic Press: New York **1982**.

5. Deisenhofer, J.; Epp, O.; Miki, K.; Huber, R.; Michel, H. *J. Mol. Biol.* **1984**, *180*, 385-398.

6. Woodbury, N. W.; Becker, M.; Middendorf, D.; Parson, W. W. *Biochemistry* **1985**, *24*, 7516-7521. In this work, the photosynthetic reaction center in the related bacterium *Rhodopseudomonas sphaeroides* was studied.

7. Rehm, D.; Weller, A. *Isr. J. Chem.* **1970**, *8*, 259-271.

8. Miller, J. R.; Beitz, J. V.; Huddelston, R. K. *J. Am. Chem. Soc.* **1984**, *106*, 5057-5068.

9. Miller, J. R.; Beitz, J. V. *J. Chem. Phys.* **1981**, *74*, 6746-6756.

10. Mauk, A. G.; Scott, R. A.; Gray, H. B. *J. Am. Chem. Soc.* 1980, *102*, 4360-4363.

11. English, A. M.; Lum, V. R.; DeLaive, P. J.; Gray, H. B. *J. Am. Chem. Soc.* **1982**, *104*, 870-871.

12. Tabushi, I.; Koga, N.; Yanagita, M. *Tetrahedron Lett.* 1979, *3*, 257-260.

13. Isied, S. S.; Vassilian, A. *J. Am. Chem. Soc.* **1984**, *106*, 1732-1736.

14. Isied, S. S.; Magnuson, R. H. Schwarz, H. A. *J. Am. Chem. Soc.*

1985, *107*, 7432-7438.

15. Bolton, J. R.; Ho, T.-F.; Liauw, S.; Siemiarczuk, A.; Wan, C. S. K.; Weedon, A. C. *J. Chem. Soc. Chem. Commun.* **1985**, *1985*, 559-560.

16. Hush, N. S.; Paddon-Row, M. N.; Cotsaris, E.; Oevering, H.; Verhoeven, J. W.; Heppener, M. *Chem. Phys. Lett.* **1985**, *117*, 8-11.

17. Wasielewski, M. R.; Niemczyk, M. P.; Svec, W. A.; Pewitt, E. B. *J. Am. Chem. Soc.* **1985**, *107*, 1080-1082.

18. Franco, C.; McLendon, G. *Inorg. Chem.* **1984**, *23*, 2370-2372.

19. Leland, B. A.; Joran, A. D.; Felker, P. M.; Hopfield, J. J.; Zewail, A. H.; Dervan, P. B. *J. Phys. Chem.* **1985**, *89*, 5571-5573.

20. Ohta, K.; Closs, G. L.; Morokuma, K.; Green, N. *J. Am. Chem. Soc.* **1986**, *108*, 1319-1320.

21. McGourty, J. L.; Blough, N. V.; Hoffman, B. M. *J. Am. Chem. Soc.* **1983**, *105*, 4470-4472.

22. Simolo, K. P.; McLendon, G. L.; Mauk, M. R.; Mauk, A. G. *J. Am. Chem. Soc.* **1984**, *106*, 5012-5013.

23. McLendon, G. L.; Winkler, J. R.; Nocera, D. N.; Mauk, M. R.; Mauk, A. G.; Gray, H. B. *J. Am. Chem. Soc.* **1985**, *107*, 739-740.

24. Ho, P. S.; Sutoris, C.; Liang, N.; Margoliash, E.; Hoffman, B. M. *J. Am. Chem. Soc.* **1985**, *107*, 1070-1071.

25. Mathews, C. R.; Erickson, P. M.; Van Vliet, D. L.; Petersheim, M. *J. Am. Chem. Soc.* **1978**, *100*, 2260-2262.

26. Mathews, C. R.; Erickson, P. M.; Froebe, C. L. *Biochim. Biophys. Acta* **1980**, *624*, 499-510.

27. Yocom, K. M.; Shelton, J. B.; Shelton, J. R.; Schroeder, W. A.; Worosila, G.; Isied, S. S.; Bordignon, E.; Gray, H. B. *Proc. Natl. Acad. Sci. USA* **1982**, *79*, 7052-7055.

28. Kostic, N. M.; Margalit, R.; Che, C.-M.; Gray, H. B. *J. Am. Chem. Soc.* **1983**, *105*, 7765-7767.

29. Winkler, J. R.; Nocera, D. G.; Yocom, K. M.; Bordignon, E.; Gray, H. B. *J. Am. Chem. Soc.* **1982**, *104*, 5798-5800.

30. Nocera, D. G.; Winkler, J. R.; Yocom, K. M.; Bordignon, E.; Gray, H. B. *J. Am. Chem. Soc.* **1984**, *106*, 5145-5150.

31. Crutchley, R. J.; Shelton, J. B.; Shelton, J. R.; Schroeder, W. A.; Gray, H. B., unpublished results.

32. Crutchley, R. J.; Ellis, W. R., Jr.; Gray, H. B. *Frontiers in Bioinorganic Chemistry*, Xavier, A. V., ed. VCH Verlagsgesellschaft: Weinheim, FRG, **1986**, pp. 679-693.

33. Crutchley, R. J.; Ellis, W. R., Jr.; Gray, H. B. *J. Am. Chem. Soc.* **1985**, *107*, 5002-5004.

34. *Barry's Bible: Methods in Bioinorganic Chemistry*, 2nd ed., Pasadena, California **1981**, p. 94.

35. Schilt, A. A.; Taylor, R. C. *J. Inorg. Chem.* **1959**, *9*, 211-221.

36. Pfeiffer, P.; Werdelmann, B. *Z. Anorg. Allg. Chem.* **1950**, *263*, 31-38.

37. Ford, P.; Rudd, De F. P.; Gaunder, R.; Taube, H. *J. Am. Chem. Soc.* **1968**, *90*, 1187-1194.

38. Winter, A.; Perlmutter, H.; Davies, H. *Preparative Flat-BEd Electrofocusing in a Granulated Gel with the LKB 2117 Multiphor*, Application Note 198, revised **1980**.

39. Adler, A. D.; Longo, F. R.; Kampas, F.; Kim, J. *J. Inorg. Nucl. Chem.* **1970**, *32*, 2443-2445.

40. Doss, M. *Z. Klin. Chem. u. Klin. Biochem.* **1970**, *8*, 208-211.

41. Teale, F. W. J. *Biochim. Biophys. Acta* **1959**, *35*, 543.

42. Yonetani, T. *J. Biol. Chem.* **1967**, *242*, 5008-5013.

43. Schichman, S. *Barry's Bible: Methods in Bioinorganic Chemistry*, 2nd ed., Pasadena, California **1981**, pp. 84-85.

44. Stryer, L. J. *J. Mol. Biol.* **1965**, *13*, 482-495.

45. Leonard, J. J.; Yonetani, T.; Callis, J. B. *Biochemistry* **1974**, *13*, 1460-1464.

46. Rice, S. F.; Gray, H. B. *J. Am. Chem. Soc.* **1983**, *105*, 4571-4575.

47. Henkel, J. G.; Clarke, F. H. *Molecular Graphics on the IBM PC Microcomputer*, Academic Press: New York **1985**.

48. Takano, T. *J. Mol. Biol.* **1977**, *110*, 537-568.

49. Takano, T. *J. Mol. Biol.* **1977**, *110*, 569-584.

50. Stynes, H. C.; Ibers, J. A. *J. Inorg. Chem.* **1971**, *10*, 2304-2308.

51. LKB Ampholine polyacrylamide gel plates (PAG plates) were used as per instructions of the supplier. A pH range of 3.5 - 9.5 (LKB #1804-101) was employed.

52. After heme extraction, 17.2 mg (A_{280} = 0.355, ε = 15.8 $mM^{-1}cm^{-1}$, 17200 m.w.,[53] 45 mL) of protein were available for reconstitution. The zinc mesoporphyrin was inserted, and following centrifugation and a Sephadex G-25-80 column, 17.5 mg (A_{280} = 0.403, 40 mL) were recovered. The amount of reconstituted protein is actually in apomyoglobin equivalents as the zinc porphyrin is not included in the calculation.

53. Edmundson, A. B.; Hirs, C. H. W. *J. Mol. Biol.* **1962**, *5*, 663-682.

54. Hanania, G. I. H.; Yeghiayan, A.; Cameron, B. F. *Biochem. J.* **1966**, *98*, 189-192.

55. Bowen, W. J. *J. Biol. Chem.* **1949**, *179*, 235-245.

56. Sundberg, R. J.; Gupta, G. *Bioinorg. Chem.* **1973**, *3*, 39-48.

57. Emission experiments were conducted by J. L. Marshall; many thanks.

58. Hoffman, B. M. *J. Am. Chem. Soc.* **1975**, *97*, 1688-1694.

59. Kalyanasundaram, K.; Neumann-Spallart, M. *J. Phys. Chem.* **1982**, *86*, 5163-5169.

60. Zang, L.-H.; Maki, A. H., unpublished results. These experiments utilize optically detected magnetic resonance (ODMR) and involve the direct measurement of the Mb(^{3}ZnP*) lifetime (λ_{max} = 698 nm) in frozen matrices.

61. Vanderkooi, J. M.; Adar, F.; Erecinska, M. *Eur. J. Biochem.* **1976**, *64*, 381-387.

62. Conrad, R. H.; Brand, L. *Biochemistry* **1978**, *7*, 777-787. κ is the dipole-dipole orientation factor, N_A is Avogadro's number (mol^{-1}), n is the refractive index of the medium, τ is the natural lifetime of the donor, and R is the distance between the donor and acceptor (cm). $\int F_D(\lambda)\varepsilon_A(\lambda)\lambda^4 d\lambda$ is the overlap integral ($cm^6\,mol^{-1}$) where $F_D(\lambda)$ describes the probability of donor emission as a function of wavelength and $\int F_D(\lambda)d\lambda = 1$. $\varepsilon_A(\lambda)$ is the molar decadic extinction spectrum of the acceptor ($cm^2\,mol^{-1}$). The overlap integral was calculated by normalizing the donor emission spectrum and multiplying F_D by the acceptor extinction

coefficient and λ^4 at each wavelength. The product was plotted vs. λ and the area is the value of the overlap integral.

63. Navon, G.; Sutin, N. *Inorg. Chem.* **1974**, *13*, 2159-2164. The lowest-lying excited state, $^4T_{1g}$, in the $Ru^{3+}N_6$ complex $a_6Ru(ClO_4)_3$ is at 435 nm (23000 cm^{-1}). The $a_5Ru(His)^{3+}$ spectrum is red-shifted with respect to the a_6Ru^{3+}, lowering the $^4T_{1g}$ energy level to as little as 16700 cm^{-1} (600 nm). Beyond 650 nm, the extinction coefficients are negligible.[55]

64. Dexter, D. L. *J. Chem. Phys.* **1953**, *21*, 836-850.

65. Ideally, direct observation of an electron-transfer product, either Ru(II) or ZnP^+, would provide unequivocable evidence for this conclusion. These species, however, have not been spectroscopically observed in the $a_5Ru(His)Mb(ZnP)$ systems.

66. Winkler, J. R., personal communication. a). Work with zinc-substituted cytochrome *c* reveals that the slow component phosphoresces, a feature not expected in the reverse electron-transfer reaction. b) The amount of impurity appears to correspond to the number of fractions pooled together to make-up the sample..

67. A more stringent selection of elution fractions lowers the minor component contribution.

68. Samples were treated with sodium dithionite in an inert atmosphere box. Excess dithionite was removed by four cycles of concentration and dilution with an Amicon ultrafiltration unit.

69. Ringe, D.; Petsko, G. A.; Kerr, D. E.; Ortiz de Montellano, P. R. *Biochemistry* **1984**, *23*, 2-4.

70. Hartmann, H.; Parak, F.; Steigemann, W.; Petsko, G. A.; Ringe

Ponzi, D.; Frauenfelder, H. *Proc. Natl. Acad. Sci. U.S.A.* **1982**, *79*, 4967-4971.

71. Ringe, D.; Petsko, G. A. *Prog. Biophys. Molec. Biol.* **1985**, *45* 197-235.

72. Marcus, R. A.; Sutin, N. *Biochim. Biophys. Acta* **1985**, *811*, 265-322.

73. Hush, N. S. *Coord. Chem. Rev.* **1985**, *64*, 135-157.

74. Beratan, D. N.; Onuchic, J. N.; Hopfield, J. J. *J. Chem. Phys.* **1985**, *83*, 5325-5329.

75. Scheidt, W. R. *Acc. Chem. Res.* **1977**, *10*, 339-345.

76. Ayrovainen, M. Candidacy report, California Institute of Technology **1984**, p. 5.

77. Ringe, D.; Petsko, G., unpublished results.

78. Hopfield, J. J. *Proc. Natl. Acad. Sci. USA* **1974**, *71*, 3640-3644.

79. Beratan, D. N., personal communication.

80. Liang, N.; Pielak, G. J.; Mauk, A. G.; Smith, M.; Hoffman, B. M. *Proc. Natl. Acad. Sci. U.S.A.*, in press.

81. Mayo, S. L.; Ellis, W. R., Jr.; Crutchley, R. J.; Gray, H. B. *Science* **1986**, *233*, 948-952.

82. Peterson-Kennedy, S. E.; McGourty, J. L.; Hoffman, B. M. *J. Am. Chem. Soc.* **1984**, *106*, 5010-5012.

83. Poulos, T. L.; Mauk, A. G. *J. Biol. Chem.* **1983**, *258*, 7369-7373.

84. Salemme, F. R. *J. Mol. Biol.* **1976**, *102*, 563-568.

85. Poulos, T. L.; Kraut, J. *J. Biol. Chem.* **1980**, *255*, 10322-10330.

86. Calcaterra, L. T.; Closs, G. L.; Miller, J. R. *J. Am. Chem. Soc.***1983**, *105*, 670-671.

87. Miller, J. R.; Calcaterra, L. T.; Closs, G. L. *J. Am. Chem. Soc.*1984, *106*, 3047-3049.

88. Verhoeven, J. W.; Paddon-Row, M. N.; Hush, N. S.; Oevering, H.; Heppener, M. *Pure & Appl. Chem.* **1986**, *58*, 1285-1290.

89. Heitele, H.; Michel-Beyerle, M. E. *J. Am. Chem. Soc.* **1985**, *107*, 8286-8288.

90. Joran, A. D.; Leland, B. A.; Geller, G. G.; Hopfield, J. J.; Dervan, P. B. *J. Am. Chem. Soc.* **1984**, *106*, 6090-6092.

91. Larsson, S. *J. Am. Chem. Soc.* **1981**, *103*, 4034-4040.

92. Deisenhofer, J.; Epp, O.; Miki, K.; Huber, R.; Michel, H. *J. Mol. Biol.* **1984**, *180*, 385-398.

93. Karplus, M.; McCammon, J. A. *Sci. Amer.* **1986**, *254(4)*, 42-51.